ABSTRACT

LOEWENTHAL, ETHAN. Low-Order Modeling of Wing-Tip Vortices Using an Augmented Vortex Lattice Method. (Under the direction of Dr. Ashok Gopalarathnam).

Wing-tip flow effects become increasingly significant in the prediction of forces and moments on a wing as the aspect ratio decreases. Similar to the attached leading-edge vortex of delta wings, the wing-tip vortex is characterized by a separated flow structure that is not included in conventional vortex lattice method (VLM) models. These models assume fully-attached flow at the tip, and therefore fail to capture what portion of the wing-tip vortex exists as a free vortex upstream of the trailing edge. Even at small angles of attack, some degree of the shear layer separation that feeds the free tip vortex can and generally does occur. The most significant consequence of this attached vortex structure is the increased suction, and therefore, normal force developed near the wing tips. This increased normal force results in a supplementary lift known as "vortex lift" (and "vortex drag"), which acts in addition to the "linear lift" associated with fully-attached flow. For low-aspect-ratio wings this effect on lift, as well as all forces and moments, is significant.

The current work consists of a low-order, potential-flow model designed to capture the geometry and strength of the free tip vortex along the wing tip itself, as well as the amount of vorticity that remains bound to the wing tip. Many augmented VLMs–both steady and unsteady–have addressed these separated flow structures on the leading edges of delta wings, as well as on wing tips. This model is distinguished from those VLM models by its allocation of vorticity between the wing tip and the tip vortex at each chordwise position. The amount of vorticity that remains bound is controlled by defining a maximum allowable vorticity that may be supported by the tip edge. This value may be based on the particular tip geometry, as well as other parameters, such as the Reynolds number. Where the total vorticity along the tip exceeds this value, vorticity is allocated such that the balance is shed to feed the free vortex. This paper discusses the model, as well as its ability both to position the tip vortex and to predict forces and moments on low-aspect-ratio wings more accurately than a conventional VLM.

The model has the ability to represent the free shear layer using elements that are straight lines (planar shear layer), any portion of a circle or a spiral, and this paper presents results from the planar shear layer. Because this geometry performed well, generally, but did not converge in sideslip, an alternate shear layer geometry represented by 3/4 of a circle is presented in Appendix A. For both shear layer geometries, the model demonstrates good initial agreement with the expected lift distribution typical of vortex lift, as well as promising initial agreement with total lift, drag and pitching moment from experimental work. Rolling-moment prediction by the curved shear layer also showed good initial agreement, however no rolling-moment results are presented for the planar shear layer, due to a failure to converge in sideslip. For both geometries, it is shown that the forces and moments predicted by the low-order model can be "throttled" by controlling the maximum allowable bound vorticity along the wing tip.

Low-Order Modeling of Wing-Tip Vortices Using an Augmented Vortex Lattice Method

by
Ethan Loewenthal

A thesis submitted to the Graduate Faculty of
North Carolina State University
in partial fulfillment of the
requirements for the degree of
Master of Science

Aerospace Engineering

Raleigh, North Carolina

2019

APPROVED BY:

Dr. Andre Mazzoleni

Dr. Venkateswaran Narayanaswamy

Dr. Ashok Gopalarathnam
Chair of Advisory Committee

DEDICATION

To my parents.

BIOGRAPHY

Ethan Loewenthal was born in Chapel Hill, North Carolina in 1978. He earned a bachelor of science degree in civil engineering from Brown University in 2002, and then held several jobs over the subsequent 14 years in the fields of structural engineering, blacksmithing, carpentry and agriculture. His first job was as a structural engineer at KCI Technologies in Raleigh, NC, analyzing and designing modifications for radio towers. Following this initial foray into engineering, he worked as an apprentice to Bill Brown, blacksmith artist and owner of Anvil Arts in Linville Falls, NC, helping him build a set of gates for the North Carolina Arboretum in Asheville, NC. In 2006, he moved back to Chapel Hill, NC, where he worked as a self-employed carpenter, building decks fences and a set of outrageously large rocking chairs for High Point University. Returning to structural engineering in 2008, he worked for four years at Barlow Engineering in Raleigh, NC, analyzing and designing modular homes. His next job was as a farm manager, starting and running Funny Girl Farm in Durham, NC. There, he managed a group of farmers, raised vegetables, shiitake mushrooms and free-range eggs, and helped run the farm stand. After handing the farm off to his team, he enrolled at North Carolina State University in the Mechanical and Aerospace Engineering department, eventually working under the advisement of Dr. Gopalarathnam in the Applied Aerodynamics Group. After graduating in the summer of 2019 Ethan plans to find work as an aerospace engineer in the Raleigh area.

ACKNOWLEDGEMENTS

I would like to thank and acknowledge Dr. Gopalarathnam for his direction and wisdom during the process of building this model, troubleshooting problems and interpreting the results. He has been as an excellent teacher and a thoughtful advisor, and I am grateful to have found a place in his research group. During the many snags I hit during the course of my research, he was a steady hand, ready and interested to tackle the next question, and always with a sense of joy and wonder for the material.

I would also like to thank the other two members of my committee: Dr. Narayanaswamy and Dr Mazzoleni for their excellent teaching. Their classes challenged and inspired me, and their patience and interest in answering my numerous questions was a valuable part of my education.

TABLE OF CONTENTS

LIST OF FIGURES

NOMENCLATURE

α	Angle of attack
Æ	Aspect ratio
β	Sideslip angle
$_P$	Pressure coefficient
Γ	Circulation
Λ	Quarter-chord wing sweep
ρ	Air density
b_{ref}	Wing reference span
c	Chord length
C_F	Generic force coefficient
c_{ref}	Wing reference chord
C_D	Wing drag coefficient
C_L	Wing lift coefficient
C_l	Lift Coefficient
C_{Mx}	Wing rolling moment coefficient
C_{My}	Wing pitching moment coefficient
LAR	Low-aspect-ratio
LEV	Leading-edge vortex
LOM	Low-order model presented in the current work

Re	Reynolds number
S_{ref}	Wing reference area
V	Total local velocity
V_∞	Free-stream velocity
V_{ind}	Induced velocity
VLM	Vortex lattice method

Chapter 1

Introduction

Wing-tip vortices have been studied extensively, both in the immediate vicinity of the wing and in the far-field. Much of the research has focused on the flow field aft of the trailing edge of the wing [4, 5, 6, 7], in particular on the persistence of tip vortices in the far-field. Tip vortex behavior in this far-field region is valuable in predicting the flow field encountered by a following aircraft and is an important factor in determining how close one aircraft can follow another. However, a smaller number of low-order models have addressed the tip vortex along the wing tip itself. And, it appears that no models thus far have allocated vorticity between what remains bound to the wing tip and what is shed to feed the tip vortex using the methodology of the model discussed in this paper. The strength and location of this flow structure immediately adjacent to the wing and how it affects forces and moments on the wing are inherently more significant for low-aspect-ratio (LAR) wings.

LAR wings are finding increased use by micro air vehicles (MAVs) because of inherent advantages over higher-aspect-ratio wings in this particular flight realm. They are more maneuverable due to a low rolling moment of inertia, and can have very high stall angles of attack due to strong interaction between the leading-edge flow and the tip vortices. DeVoria and Mohseni demonstrated stall angles of as high as 40° for an aspect ratio ($\mathcal{R}$) of 0.75 [8]. And, with the increased prevalence of MAVs, low-order models that accurately capture tip effects are becoming more important. This is particularly true in the preliminary design stages when a large number of analyses are used to study a large sweep of flight conditions. The low-order model presented in this paper was designed with this purpose in mind.

1.1 Shortcomings of a Conventional VLM in Modeling Low-Aspect-Ratio Wings

When applied to thin lifting surfaces operating in the linear regime, the low-order panel method known as the vortex lattice method (VLM), as outlined by Katz and Plotkin [9], works well to predict forces and moments, as well as the flow-field around the lifting surface, including the strength and location of the wing-tip vortices. In this regime, the angle of attack and sideslip angle are small, and the boundary layer is generally thin and attached. However, there is an inherent discrepancy between the tip flow in a conventional VLM and the actual flow in the tip region.

A conventional VLM models fully-attached flow along the wing tips with the origin of the wing-tip vortex located at the trailing edge, while ample research demonstrates that the actual tip-vortex origin can be located at a point upstream of the trailing edge, even at small angles of attack. Using helium bubble flow visualization, Engel [3] studied the flow around the tip of a wing with a NACA 0012 airfoil and aspect ratios of 2.5 and 3, at Reynolds numbers ranging from 130,000 to 335,000. He confirmed that multiple vortical structures develop and separate from the wing tip well ahead of the trailing edge, and track inboard over the suction side of the wing with downstream distance. Studying angles of attack ranging from 2.5° to 7.5°, he found that the main vortex origin was located between 40% and 60% of the chord downstream from the leading edge ($x = 0.4c$ and $x = 0.6c$, respectively), with the origin moving closer to the leading edge as angle of attack increased. Additionally, a secondary vortex origin was located as close as 0.05c from the leading edge, and that vortex merged with the main vortex downstream.

Francis and Kennedy found that the tip-vortex roll-up process originated within just 0.05c downstream of the leading edge. Using a hot-wire anemometer to measure the flow field around a wing with a NACA 64009 airfoil and a blunt tip at an angle of attack of 4° and a Reynolds number of 247,000 they produced streamline projections at multiple cross-planes along the wing-tip chord. The plots confirm some degree of separated flow as far upstream as x = 0.05c and a separated wing-tip vortex on the suction side of the wing at least as far upstream as x = 0.6c, well ahead of the trailing edge [10].

Work by Hoffman and Velkoff also confirms that the tip-vortex origin is upstream of the trailing edge. They used flow traces to visualize the flow and find the point of tip-flow separation on blunt-tipped helicopter rotor blades at a Reynolds number of 80,000. They found that the tip-vortex origin was located at a point between x = 0.3c and x = 0.7c, with the origin moving towards the leading edge with increasing pitch in the range of 0° to 16° [11].

These studies affirm a central premise of the current work: that the tip-vortex origin is located upstream of the trailing edge, and therefore, a conventional VLM lacks the capability to capture the effects of this separated flow. Moreover, the tip vortex typically consists of multiple discrete vortical structures that initiate at points even closer to the leading edge and then coalesce as they contribute vorticity to one main vortex. Evidence of these secondary vortical structures along the tip, rather than at a single point, motivated the basic geometry of the separated vortical flow used in the current work. To capture these flow phenomena the LOM is designed for vorticity to be shed along some or all of the wing-tip chord in a sheet of vorticity, rather than from a single point. And, the maximum amount of vorticity that remains bound along the tip can be specified uniquely for each chordwise lattice position. The following subsection describes the basic elements of the low-order model in the current work (LOM).

1.2 The Model

The LOM is based on a simplified interpretation of the separated flow structure along the wing tip. At each chordwise position along the wing tip some portion of the total vorticity may be released into a free shear layer that feeds a single free tip vortex. As illustrated in Figure 1.1

and as described in the following chapter, the shear layer and tip vortex are represented by a single row of quadrilateral vortex rings. The number of straight line segments that define the sides of the ring may be specified such that the sheet has a lower fidelity, flat geometry, or a more realistic curved geometry. In this paper, a flat geometry (single line segment) is used, however an alternate geometry represented by 3/4 of a circle is considered and discussed in Appendix A. One side of each ring is bound to the wing tip and the opposite side represents the tip vortex. As vorticity is shed along the wing tip, the strengths of the vortex rings increase with downstream distance, thus modeling the accumulation of vorticity in the tip vortex. The amount of vorticity that is shed at each chordwise position along the wing tip is dependent upon the maximum allowable vorticity that is set for each position. This quantity is thought to be a function of tip geometry and likely Reynolds number, however the best method to determine this value remains open at this time. The model iterates to find a solution by adjusting the tip-vortex position to follow a streamline and then recalculates all vortex strengths, such that the boundary conditions are met. Locating the tip vortex along a streamline is consistent with a force-free wake. Once the model converges on a solution, the strengths of all bound vortex filaments (including the shear layer elements bound to the tip) are known and the forces and moments on the wing can be calculated. A key assumption of the model is that although this flow separation is fundamentally a viscous phenomenon, the flow does not involve significant viscous dissipation, making the inherently inviscid VLM a suitable base for the model.

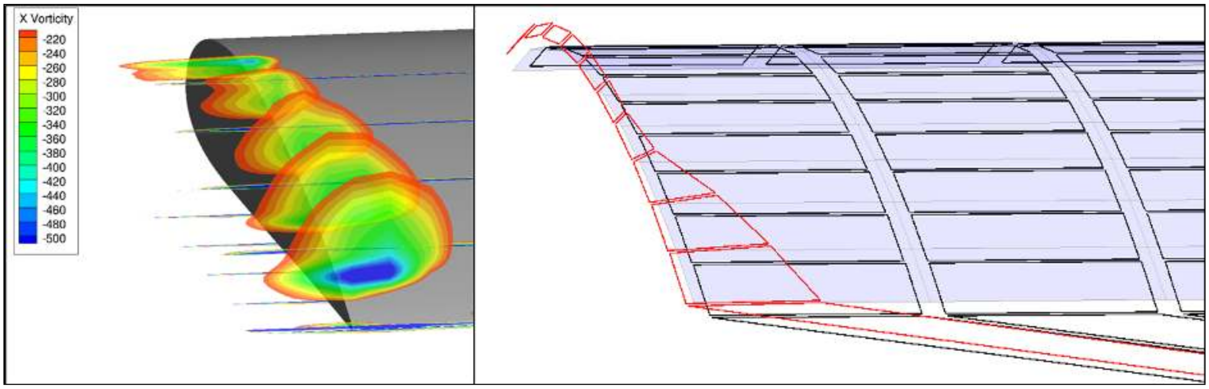

Figure 1.1: Left: tip vortex (x-vorticity or chordwise vorticity) from CFD, Right: LOM with flat shear layer geometry option; light blue: camber surface; red: shear layer and tip-vortex filaments; black: bound vortex filaments (typical of conventional VLM); gaps between vortex rings shown only for clarity; actual elements are coincident. Wing: NACA 4415 airfoil, blunt tip, $\Lambda = 0°$, $\alpha = 5°$, $\beta = 0°$.

The main consequence of this free vortex located in the immediate vicinity of the wing is vortex lift, which will be defined and discussed in a subsequent section of this chapter. First, it is important to recognize other augmented VLMs that attempt to capture these separated vortical flows and how the allocation of vorticity used in the LOM distinguishes it from those augmented models.

1.3 Other VLMs Augmented to Capture Separated Vortical Flows

Numerous VLM models have been augmented to capture the separated vortical flows off wing edges. Generally speaking, these models use supplementary vortex sheets (vortex rings or filaments) that emanate from the leading edges and/or wing tips, and are located such that they follow the local velocity. In this sense, these vortex sheets are treated in the same manner as the vortex wake that emanates from the trailing edge in a conventional VLM that allows for roll-up of the wake.

In the steady models, as in the current work, the program iterates to find a solution at which the boundary conditions are met and the vortex rings or filaments are located along streamlines. Many of these models are designed to address only the separated vortical flows along the leading edges of delta wings, such as that of Zhu et al [12]. Other similar work includes that of both Kandil et al [13] and Dodbele and Plotkin [14]; each of these groups created steady VLM models designed for multi-element delta wing configurations. In these models the critical aspect that differentiates them from the current work is the assumption that these edges are sharp and therefore cannot support any bound vorticity. In other words, the Kutta condition is enforced, and there is no bound vorticity along these edges.

Enforcing the Kutta condition along wing leading edges and/or wing tips in these augmented VLMs is common. This includes unsteady VLMs designed to capture these flows, such as that of Konstadinopoulos et al [15]. And, while not a VLM, the work of Brown and Michael [16] was an analytical model designed to model leading-edge vortices on slender delta wings. Both of these models assumed the Kutta condition along the leading edges.

Of those augmented VLM models, perhaps the most similar model to the LOM presented in this paper is that of Levin and Katz [17]. In their work an unsteady VLM accounts for the radius of curvature of the leading edges of delta wings by adjusting the amount of vorticity shed along the leading edges. However, it is not clear what particular mechanism is used to determine the magnitude of the shed vorticity at each time step. Furthermore, this capability is not modeled in the cited work, and instead the Kutta condition is assumed.

Relatively fewer augmented VLMs address separated flow along the wing tips. One example is that of Belotserkovskii [18] who created a steady VLM that modeled shed vorticity from the wing tips in the form of separate filaments that remain independent as they flow downstream. This configuration is distinct from the current work, which dictates a vortex ring geometry that forces all shed vorticity to accumulate into a single main vortex. Furthermore, the wing tips in Belotserkovskii's model are assumed sharp, and therefore, again, the Kutta condition is enforced.

1.4 Vortex Lift

Vortex lift is a result of the additional suction associated with a vortex in the near vicinity of a wing surface, and is a primary mechanism by which wing-tip vortices play an increasingly larger role as Æ decreases. The most common realm in which vortex lift is encountered is on the leading edges of highly swept delta wings, which depend on this type of lift generation at lower speeds. Designed for supersonic flight, these wings must have sharp leading edges to minimize wave drag. However, such sharp leading edges result in leading-edge flow separation in the subsonic regime at all but the smallest angles of attack, along with the associated lift reduction and drag increase. Because these aircraft must be able to generate sufficient lift at subsonic speeds in order to accommodate landing and take-off, they require some other mechanism to generate lift while contending with separated flow along the leading edges. The solution is the attached leading-edge-vortex (LEV).

It is widely accepted that the stability of attached LEVs depends on the removal of vorticity by an axial flow. As a shear layer separates off the leading edge of a wing, it may roll up to form a free vortex that accumulates vorticity. If there is no mechanism to remove vorticity, the LEV grows unstable, detaches and convects downstream. However, if a sufficient axial flow exists, then sufficient vorticity is advected along the vortex—along the leading edge in the case of a delta wing—to prevent the buildup of vorticity that would cause instability of the LEV. Wong et al [19] affirmed this concept of a vorticity budget using a low-order analytical model that properly accounted for the amount of vorticity contained in the LEV, as well as the amount of vorticity advected with the axial flow. The results were successfully validated against a flat plate delta wing in a tow tank at a Reynolds number of 260,000, using particle image velocimetry (PIV) and four-dimensional particle-tracking velocimetry (4-D-PTV) to track the vorticity transport.

In the biological realm, LEVs stabilized with spanwise flow may be achieved with the particular flapping kinematics utilized by insects, such as the hawkmoth studied by Ellington et al [20] or fish tails as studied by Borazjani and Daghooghi [21]. Another mechanism to produce sufficient axial flow in attached leading-edge vortices is a highly swept leading edge. Videler et al [22] performed water tunnel testing on a model of a swift wing at very low Reynolds numbers (3750 and 37,500) and found attached LEVs at angles of attack as low as 5° on the 60°-sweep outboard portion of the wing, known as the "hand wing." They proposed that the hand wing may be so highly swept to produce vortex lift, as opposed to the linear lift produced by the more inboard "arm wing." He offered that such vortex lift may aid birds, in general, in high-angle-of-attack landings.

For aircraft, the common planform used for wings designed to produce vortex lift at low speeds is the delta wing. For these highly swept wings, which typically have sharp leading edges, the amount of vorticity that can be held by the leading edge is very nearly zero, meaning that there is essentially none of the leading-edge suction force predicted by a potential flow model that assumes fully-attached flow. Instead, there is a substantial increase in normal force in the vicinity of the leading-edge vortex that increases total lift beyond what potential flow predicts, albeit with a substantial increase in drag as well. The left side of Figure 1.2 illustrates this concept that vortex lift can be thought of as simply an increment in addition to the lift resulting from fully-attached flow. And, the lift distribution indicative of substantial vortex lift is quite different from that resulting from fully-attached flow, as illustrated on the right side of Figure 1.2. This distinctive lift distribution will be used in Chapter 3 to interpret results from the LOM.

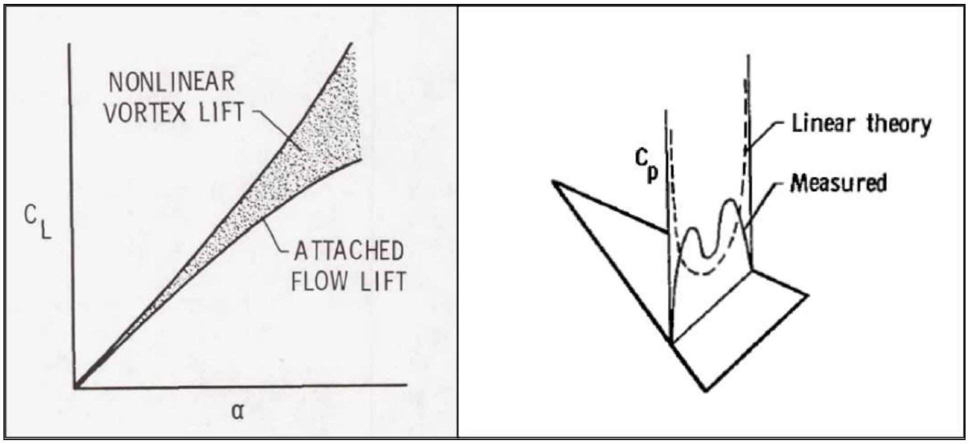

Figure 1.2: Left: The nonlinear vortex lift increment acts in addition to lift associated with attached flow [1]. Right: typical vortex lift distribution for highly swept delta wing versus that predicted by linear model [2].

This understanding of attached LEVs can be extended to attached wing-tip vortices, as demonstrated by Lamar's [23] extension of Polhamus' leading-edge suction analogy [2] to wing tips. Polhamus demonstrated that for sharp leading edges the leading-edge suction force predicted by a potential flow model could be used to predict vortex lift by turning the suction force direction from chordwise to normal to the wing upper surface. A key assumption of this model is that there is sufficient leading-edge sweep to provide the axial flow necessary to stabilize the LEV. In terms of this understanding of attached LEVs and the axial flow required to stabilize them, wing tips can be thought of as the extreme sweep case of a 90° sweep of the leading edge, and therefore have the maximum amount of axial flow available to stabilize the tip vortex. Lamar's experimental work on LAR wings demonstrated very well the concept that, like the vortex lift resulting from LEVs, vortex lift resulting from wing-tip vortices can be thought of as a lift force increment that acts in addition to attached-flow lift. As described by Lamar, "the suction analogy concept is not limited to vortex flows around the leading-edge but can be applied wherever singularities in the potential-flow-induced velocities produce an edge force" [24]. Bradley et al [25] compared total lift predicted by the work of Polhamus and Lamar's extension to side edges and found good agreement with experimental results for LAR wings of aspect ratios ranging from 0.5 to 2. Furthermore, their plots demonstrated that as Æ decreases, not only does vortex lift comprise more of the total lift, but vortex lift along the wing tips comprises more of the total vortex lift.

And, the suction analogy is not limited to a binary interpretation. Some leading-edge suction may be maintained while some of the suction force acts as a normal force. Lamar [26] was able to identify a "conservation of suction" from wind tunnel investigations of highly swept delta wings with variable leading-edge radii. He described how "part of the leading-edge thrust goes into vortex lift, and part remains as leading-edge suction." By measuring the leading-edge suction force and the normal force resulting from vortex lift, he found that the sum of these two forces was the same for wings of a given sweep angle but with different leading-edge radii, even though each force component was different. In the sense that edge suction is a direct result of bound vorticity, while normal-force suction is a result of shed vorticity that feeds an attached edge vortex, this "conservation of suction" concept serves as a validation of the allocation-of-vorticity concept used in the current work.

Further confirmation that vortex lift occurs at wing tips comes from work by Chigier and Corsiglia [27]. They performed wind tunnel experiments on a rectangular wing with NACA 0015 airfoil at an angle of attack of 12° and a Reynolds number of 95,300, and were able to clearly show suction associated with the wing-tip vortex. By plotting isobars on the upper wing surface, both the low pressure zone near the wing tip associated with the tip vortex and the leading-edge suction region associated with attached flow are clearly evident as two distinct suction regions. Furthermore, the spanwise lift distribution was found to be more rectangular than elliptical, a result of the additional vortex lift at the tip. Figure 3.9 presents CFD results from the current work on a wing at an angle of attack of 18° (Æ = 1, airfoil: NACA 0012, Re = 80,000) and provides further evidence of these two suction regions: (i) the suction resulting from the separated tip vortex above the suction side of the wing and (ii) the suction along the leading edge resulting from attached flow. These suction areas are the two lift distribution signatures to which the LOM lift distributions are compared in Chapter 3.

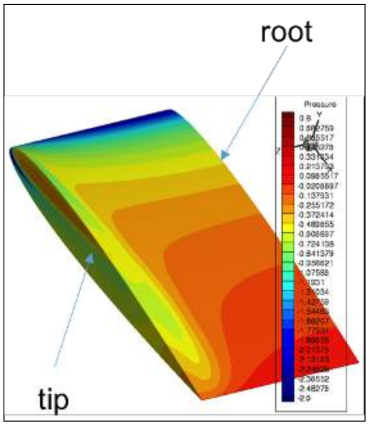

Figure 1.3: CFD results: pressure distribution on suction side of wing with NACA 0012 airfoil at 18° angle of attack, $\mathit{Æ} = 1$, Re = 80,000, demonstrating suction near tip due to free tip vortex and suction along leading edge associated with attached flow.

1.5 Distinguishing the LOM: Allocation of Vorticity

Although this proposed model pertains to steady flow, the concept of a maximum circulation that may be supported by the wing-tip edge was inspired by the leading-edge suction parameter (LESP), proposed by Ramesh et. al [28] and used to model dynamic stall. In that research, the suction at the leading edge of an airfoil undergoing pitching and plunging maneuvers was quantified as a non-dimensional parameter known as the LESP. This parameter was used in a two-dimensional discrete vortex method to predict when LEV production would initiate and terminate, based on whether LESP was less than or greater than a critical LESP value specific to the airfoil and Reynolds number. Similarly, the current three-dimensional steady flow method sets an upper limit on how much vorticity may be supported at each chordwise position along the wing tip, based on tip geometry and possibly Reynolds number, among other parameters.

The key significance of controlling the allocation of vorticity along the wing-tip edge is its effects on the location and strength of the tip vortices, which in turn have significant effects on forces and moments. Specifically, more vorticity shed results in greater vortex lift and vortex drag. Not only does this influence the total forces, but the particular distribution of these forces presents challenges in accurately predicting pitching and rolling moments. These challenges will be discussed in Chapter 3.

Luckring provided a summary of the effects of delta wing leading-edge geometry on LEV formation that is particularly helpful in understanding the significance of vorticity allocation in the current work [29]. In a project known as the “Vortex Flow Experiment 2,” wind tunnel testing was conducted on a delta wing of 65°-sweep and variable leading-edge geometry, and the effects on LEV formation were studied as a function of Mach number, Reynolds number, angle of attack and the leading-edge geometry. The results presented compare the LEV formation and location for a delta wing with either a sharp leading edge or a blunt (rounded) leading edge. On the sharp leading edge, the LEV origin is at the apex, and the LEV is located along the leading edge. While, for a blunt leading edge the origin of the attached LEV is farther downstream and is located more inboard of the leading edge.

In addition to a more downstream LEV origin for the blunt leading edge, a plot of C_P for a particular mid-span location along the blunt leading edge versus angle of attack demonstrates that some leading-edge suction, and therefore some degree of vorticity, remains bound, even downstream of the LEV origin. At low α, for which the LEV origin is outboard/downstream of the measurement point, the suction increases rapidly and nonlinearly with increasing α until a peak corresponding to the point at which the LEV origin is located at the point of measurement. As α increases further and the LEV origin moves more inboard/upstream, the suction suddenly drops, but then levels off to a value approximately half that of the peak value. This leveling-off is consistent with the concept of some vorticity remaining bound to the leading edge, even as some vorticity is shed to feed the attached LEV. Furthermore, it is consistent with the more inboard location of the LEV for the blunt leading edge, which implies some turning of the flow that would result from a boundary layer that remains attached for some portion of the turn around the leading edge. As will be discussed in Chapter 3, this more inboard location for the vortex when some vorticity remains bound to the tip is successfully demonstrated by the LOM.

As described in the previous section, the attached LEV offers an analogy to the wing-tip vortex as a fundamentally similar phenomenon. As such, these results presented by Luckring provide an excellent framework in which to understand the allocation of vorticity along a wing tip and interpret the results of the LOM in Chapter 3.

1.6 Inherent Challenges

The tip vortex's close proximity to the wing presents a significant hurdle for the LOM in achieving convergence and producing accurate results, because the immediate vicinity of the wing is an inherently challenging area in which to capture the flow phenomena for a VLM. This is due to the nonlinear nature of the irrotational vortex model used to calculate induced velocities in this and all conventional VLMs. The Biot-Savart Law prescribes an inverse relationship between the velocity induced by a vortex of strength, Γ, at a given point and the distance from that point to the vortex, as follows:

$$V_{ind} = \frac{\Gamma}{2\pi r} \tag{1.1}$$

This nonlinear relationship can produce spurious results at points very close to the wing. And, this is particularly true for coarsely-latticed wings, which are represented by fewer but stronger vortices. This suggests that a properly working model may require a higher number of lattices and therefore a greater computation time. Excessive computation times would be at odds with the low-order nature of the model and partially negate its usefulness.

Furthermore, the wing is modeled as having zero thickness, so the orientation of streamlines in this region necessarily differs from those of actual streamlines that follow the surface of a profiled wing of non-zero thickness. These differences are insignificant when calculating the velocity at a point in the far-field (and, specifically at control points and force-calculation points on the wing). However, the current model depends heavily on local velocities calculated in the immediate vicinity of the wing to accurately position the free tip vortex and associated suction force. As discussed in Chapter 3, achieving convergence of the LOM and accurately locating the tip vortex proves challenging, particularly for some scenarios in which the tip vortex is very close to the wing. The model failed to converge for many cases involving sideslip, and an alternative shear layer geometry that did converge for those cases is offered in Appendix A.

1.7 Validation of the Model

Experimental work and empirical models from five sources were used to validate the LOM. Those sources are outlined in Chapter 3. However, a preliminary discussion of the validation of forces and moments, with results from the experimental work of DeVoria and Mohseni [30] is presented here. They studied LAR wings across a large range of angles of attack and sideslip angles, for aspect ratios ranging from 0.75 to 3 at a Reynolds number of 80,000. They measured forces and moments, and used stereoscopic digital particle image velocimetry (S-DPIV) to capture the flow field.

There are inherent limitations in how precisely the LOM results should match this work, and they are as follows. First, the flow around LAR wings, generally, is commonly understood to be quite three-dimensional and characterized by significant flow separation, particularly at the higher angles of attack and sideslip angles used by DeVoria and Mohseni. Furthermore, the wings used in their work were thin, flat plates and therefore differ in at least one fundamental way from the assumptions built into the current work. Because the leading edge is thin and blunt, some degree of leading-edge separation should be expected, even at low angles of attack. And indeed, DeVoria and Mohseni observed significant leading-edge separation. They also observed leading-edge flow re-attachment induced by the strong downwash of the tip vortices. This leading-edge flow separation and subsequent reattachment was also observed in experimental work by Taira and Colonius [31] on LAR wings in an oil tow-tank at Reynolds numbers of 300 and 500. They observed separated flows from the leading edge and the wing tips with significant interaction between the two.

For purposes of validating the current work in a regime best suited to the LOM, more focus is placed on angles of attack below 10°, where leading-edge separation should play less of a role.

This approach is affirmed by Cosyn and Vierendeels [32], who performed CFD analyses of LAR wings at a Reynolds number of 100,000, using two different profiles. One wing was a flat plate and the other used an S5010 airfoil profile. The S5010 has a significantly rounded leading edge, which should support attached leading-edge flow, and therefore greater lift at a larger range of angles of attack than the flat plate. Yet, results showed very close agreement in lift and drag below angles of attack of 10° and 8°, respectively, regardless of the airfoil shape. This agreement continued up to increasing angles of attack with decreasing aspect ratios, demonstrating that for LAR wings operating at a Reynolds number near 10^5, lift and drag are not greatly affected by the particular wing profile. These results are consistent with the findings and discussion of DeVoria and Mohseni, Taira and Colonius, and Cosyn and Vierendeels, all of whom reference the influence of tip vortices in re-attaching the separated leading-edge flow for LAR wings. For purposes of validating the LOM, these findings bolster the idea that the fully-attached leading-edge flow assumed by the VLM is valid for LAR wings at these lower ranges of angle of attack. These differences are recognized and discussed in Chapter 3.

1.8 Objectives

There are three main objectives set out for the LOM in the current work:

1) ***Achieve convergence of the model across a range of angles of attack and sideslip angles, and successfully demonstrate allocation of vorticity between what remains bound to the wing tip and what is shed to feed the free wing-tip vortex***. This should give the LOM the ability to “throttle” lift and drag by controlling vorticity allocation. For example, a sharp wing tip (zero bound vorticity) should produce more vortex lift. A more rounded wing tip (more bound vorticity) should produce less vortex lift. And finally, if the maximum allowable bound vorticity is set to a sufficiently high value, the LOM should behave just as a conventional VLM with fully-attached flow.

2) ***Accurately locate the tip vortices***. Tip-vortex locations at the mid-chord and trailing edge will be compared to experimental work and an empirically-derived model. As outlined in

the “Inherent Challenges” section above, this objective presents challenges inherent to any VLM that attempts to capture separated flow in the near vicinity of the wing.

3) ***Accurately predict forces and moments***. As discussed in Chapter 3, while lift, drag and pitching moment are fairly well predicted, validation of the rolling moments could not be accomplished with the current model, due to a failure to converge. Results from an alternate shear layer geometry that does converge in sideslip is offered in Appendix A.

1.9 Layout of the Thesis

The remainder of this paper is divided into three main categories:

1) **Chapter 2: The Model**. The fundamentals of a conventional VLM are outlined, and the augmentations that distinguish the LOM are defined and discussed. The model has several modes of operation, and these are also defined and discussed.

2) **Chapter 3: Results**. The chapter begins with initial results and a number of studies that were conducted to establish the optimal modes of operation of the LOM for the validation process. The subsequent section presents the results, including comparisons to experimental results of tip-vortex locations, forces and moments. Discussions and explanations are offered, particularly how the spanwise and chordwise lift distributions help explain performance of the model and discrepancies with experimental results.

3) **Chapter 4: Conclusions**. A summary of the LOM results and validation is presented.

4) **Appendix A**. As will be presented in Chapter 3, the LOM fails to converge for many cases in the presence of sideslip. Therefore, an alternate shear layer geometry that does converge in the presence of sideslip is presented in Appendix A.

Chapter 2

The Model

The LOM presented in the current work is based on a conventional VLM and has been augmented with additional vortex filaments to model the free vortical flows that separate along the wing tips and roll up to form the wing-tip vortices. The following section first explains a conventional VLM.

2.1 A Conventional VLM

Numerical methods known as panel methods calculate a flowfield around an object by distributing mathematical singularities over its surface and enforcing a zero-normal-flow boundary condition. In the case of a thin lifting surface, such as a wing, a version of a panel method known as the vortex lattice method (VLM), as outlined by Katz and Plotkin [9], discretizes the camber surface into quadrilateral elements, on which are overlaid quadrilateral vortex rings. The leading edge of each ring is located at the panel's quarter-chord line and a collocation point is located in each ring at the panel's three-quarter-chord line. Additional quadrilateral vortex rings represent the trailing vortical wake, although these rings may be represented as horseshoe vortices if the starting vortex is assumed to trail the wing at an infinite distance downstream.

The velocity vector increment $d\boldsymbol{V}_{ind}$ induced by a vortex element $d\boldsymbol{l}$ at a point in the flow field is defined by the Biot-Savart law in vector form as follows:

$$d\boldsymbol{V_{ind}} = \frac{\Gamma}{4\pi}\frac{\boldsymbol{dl}\times\boldsymbol{r}}{|\boldsymbol{r}|^3} \tag{2.1}$$

where $\boldsymbol{r}$ is the vector from the vortex element $\boldsymbol{dl}$ to the point in the flow field.

The fundamental premise of the model is that the vortex rings represent the vorticity contained in the boundary layers on the wing surfaces and in the vortical wake, and they are each of the correct circulation strength such that the induced velocity field produces flow tangency at all collocation points and zero net vorticity along the trailing edge (the Kutta condition).

2.1.1 Calculation of the AIC Matrix and Vortex Circulation Strengths

The AIC matrix is an expression of the surface-normal component of the velocity induced at each control point by each vortex filament in the model, and is used in the following set of linear equations to solve for the strength of each vortex ring:

$$[AIC]\boldsymbol{\Gamma} = -\boldsymbol{V_\infty}\cdot\boldsymbol{n} \tag{2.2}$$

where $\boldsymbol{\Gamma}$ is a column vector of the vortex strengths, and $\boldsymbol{n}$ is a matrix of the panel normal unit vectors at the respective collocation points. The zero-normal-flow boundary condition at the collocation points is explicitly enforced by the equation. And, the Kutta condition at the trailing edge is enforced in the AIC matrix by using no induced velocity contributions from the vortex filaments along the trailing edge.

Typically, the orientation of the trailing vortices that represent the vortical wake are positioned parallel to the x-axis (chordwise), regardless of the angle of attack or sideslip angle. Because the actual wake follows local velocities and is therefore shifted and rolled up with downstream distance, this orientation along the x-axis represents a small-angle approximation that produces very similar results to an orientation that actually follows local velocities. A key benefit of this wake orientation is that the calculation of the AIC matrix—typically the most computationally expensive element—does not have to be repeated for each angle of attack and sideslip angle. As discussed later in the chapter, however, the LOM orients these trailing vortices to follow the free-stream, in part because at large α and β angles, there would be a sharp kink in the flow, inconsistent with the physical flow. Although this did increase computation time for a given orientation, it helped decrease the number of iterations required for convergence.

2.1.2 Calculation of the F Matrix and Induced Velocity at Force-Calculation Points

The F matrix is an expression of the induced velocity contributions at each of the force-calculation points, which are the mid-points of each of the vortex filaments. It is used to calculate the induced velocity at the force-calculation points, as follows:

$$[F]\boldsymbol{\Gamma} = \boldsymbol{V_{ind}} \tag{2.3}$$

2.1.3 Calculation of Loads

With $\boldsymbol{\Gamma}$ and the induced velocity at each force-calculation point known, the forces and moments on the wing can be calculated by applying the Kutta-Joukowski theorem to each bound vortex filament and summing the forces on all segments:

$$\boldsymbol{V} = \boldsymbol{V_\infty} + \boldsymbol{V_{ind}}$$

$$\boldsymbol{F} = \rho \boldsymbol{V} \times \boldsymbol{\Gamma} \tag{2.4}$$

The forces can then be converted into lift, drag and side-force coefficients as follows:

$$|F| = |\rho \boldsymbol{V} \times \boldsymbol{\Gamma}| = C_F \left(\frac{\rho |\boldsymbol{V_\infty}|^2}{2} \right) S_{ref}$$

$$C_F = \left(\frac{2}{S_{ref}}\right)\sum_{n=1}^{k}\left(\frac{\boldsymbol{V_n}\times\boldsymbol{\Gamma_n}}{|\boldsymbol{V_\infty}|^2}\right) \tag{2.5}$$

where k is the total number of vortex filaments.

The moment coefficient calculations begin by first calculating the vector $\boldsymbol{r}$ representing the moment arms from the reference point of the wing to each vortex filament mid-point, as follows:

$$\boldsymbol{r} = \boldsymbol{r_{vortex}} - \boldsymbol{r_{ref}}$$

where $\boldsymbol{r_{vortex}}$ is the vector from the origin to the vortex filament center, and $\boldsymbol{r_{ref}}$ is the vector from the origin to the wing reference point. Then, with the moment arms known, the moments can be calculated as follows:

$$|M| = |\rho(\boldsymbol{r}\times(\boldsymbol{V}\times\boldsymbol{\Gamma})\cdot\boldsymbol{n}| = C_M\left(\frac{\rho|\boldsymbol{V_\infty}|^2}{2}\right)l_{ref}S_{ref} \tag{2.6}$$

where $\boldsymbol{n}$ is the appropriate unit vector and l_{ref} is the appropriate reference length for the particular moment axis. Solving for the moment coefficients gives:

$$C_{M_x} = \left(\frac{2}{b_{ref}S_{ref}}\right)\sum_{n=1}^{k}\left(\frac{(\boldsymbol{r_n}\times(\boldsymbol{V_n}\times\boldsymbol{\Gamma_n}))\cdot\boldsymbol{i}}{|\boldsymbol{V_\infty}|^2}\right) \tag{2.7}$$

$$C_{M_y} = \left(\frac{2}{c_{ref}S_{ref}}\right)\sum_{n=1}^{k}\left(\frac{(\boldsymbol{r_n}\times(\boldsymbol{V_n}\times\boldsymbol{\Gamma_n}))\cdot\boldsymbol{j}}{|\boldsymbol{V_\infty}|^2}\right) \tag{2.8}$$

$$C_{M_z} = \left(\frac{2}{b_{ref}S_{ref}}\right)\sum_{n=1}^{k}\left(\frac{(\boldsymbol{r_n}\times(\boldsymbol{V_n}\times\boldsymbol{\Gamma_n}))\cdot\boldsymbol{k}}{|\boldsymbol{V_\infty}|^2}\right) \tag{2.9}$$

2.2 Augmentation to the Conventional VLM and Vorticity Allocation

The LOM presented in the current work is based on a conventional VLM and has been augmented with additional vortex filaments to model the free vortical flows that separate along the wing tips and roll up to form the wing-tip vortices. Figure 2.1 presents a sample configuration of the supplementary vortex rings (red) on the left tip of an uncambered wing modeled with three chordwise lattices. In this example, the wing has a positive angle of attack and a positive sideslip angle.

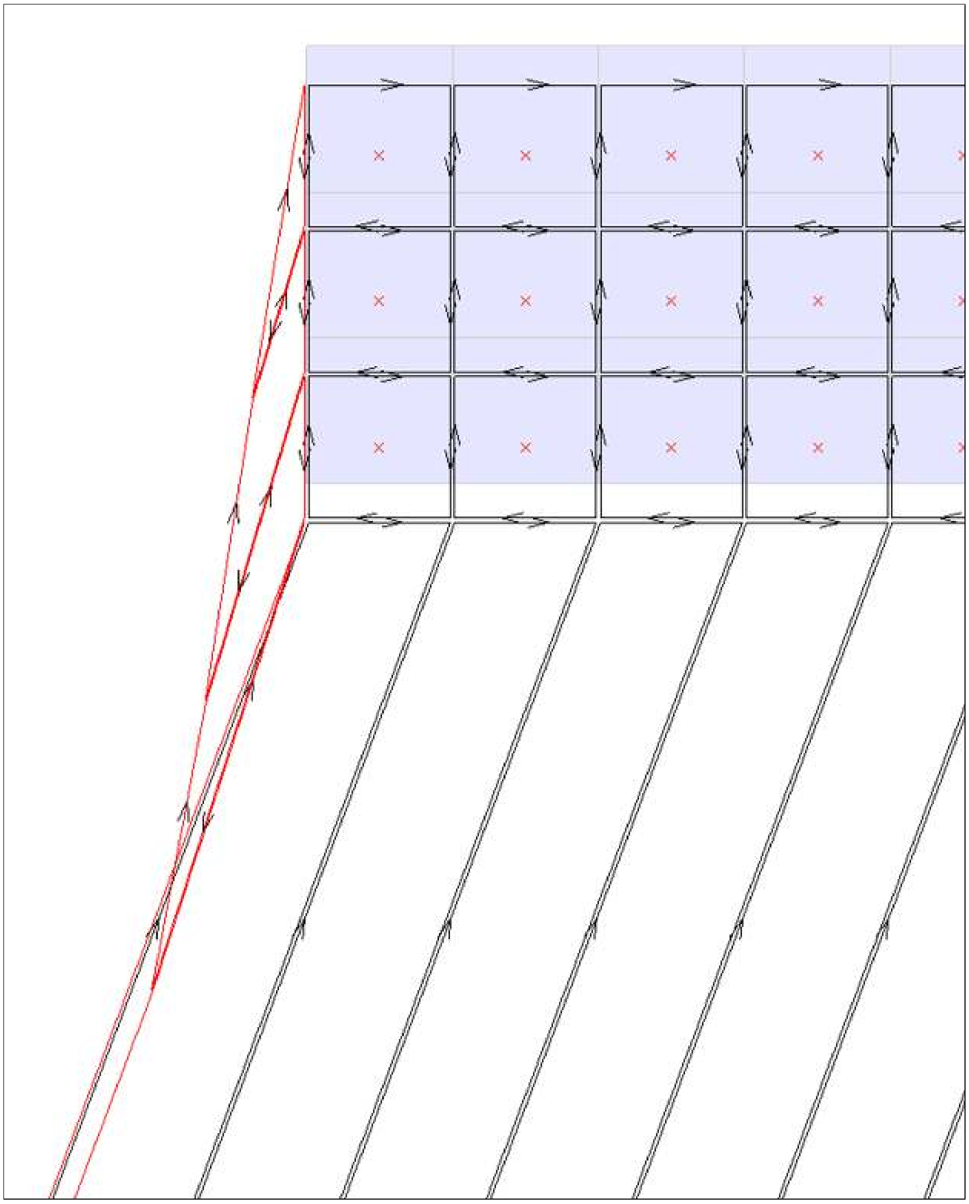

Figure 2.1: Representation of the supplementary free shear layer and tip-vortex filaments (red) on the left tip of a rectangular wing. light blue: camber surface; black: bound vortex filaments (typical of conventional VLM); gaps between vortex rings shown only for clarity; actual filaments are coincident.

In early work, it was found that convergence could be difficult to achieve for certain combinations of angle of attack and sideslip, and therefore a critical change was made to the wake orientation in the LOM. As described above, it is common for a conventional VLM to model the wake as parallel to the x-axis, regardless of the direction of the free-stream. However, it was found that by orienting the trailing vortices such that they follow the free-stream, as illustrated in Figure 2.1, convergence could be achieved with fewer iterations. This orientation also adds some fidelity to the LOM by eliminating what would be an unrealistic kink in the tip vortices at the trailing edge.

The following two subsections address the two main consequences of introducing these supplementary vortex rings:

1. There must be a method to allocate vorticity and define the strengths of the free vortex rings along the tip in what has now become an underdetermined problem.
2. Because the free vortex positions are not known apriori, the program must iterate to find a solution.

2.2.1 Vorticity Allocation and SVP

For purposes of understanding the flow of vorticity along the wing surface and in the free shear layer, it is important to note that the gaps between rings are shown for clarity, and that the vortex filaments of adjacent rings are coincident in the actual model. Along a given boundary between rings, the net vorticity is the vector sum of those two filaments. Therefore, the full magnitude of a given vortex ring's strength is only realized where it does not coincide with another ring, such as at the leading edge of the wing.

With this understanding in mind, the flow of vorticity in two critical areas can be addressed: (i) the free shear layer represented by the supplementary vortex rings and (ii) the trailing edge of the wing. First, in the free shear layer, one can see how the differences in the circulation strength of adjacent vortex rings would result in non-zero "tributary" elements that either add to or remove vorticity from the main tip vortex. Generally speaking, the strength of each vortex ring in this free shear layer increases with downstream distance, thus creating a net vorticity flow direction that acts away from the wing tip and towards the free tip vortex. This flow pattern is consistent with the known accumulation of vorticity in the main vortex, as described in Chapter 1.

In the second area, the trailing edge of the wing, it is commonly understood that the Kutta condition must be enforced. In fact, that is a critical boundary condition that is required in order to solve what would otherwise be an underdetermined problem. In a conventional VLM, as in the current work, the Kutta condition along the trailing edge is enforced by simply assigning a circulation value to each horseshoe vortex in the wake that is equal in magnitude to its bound neighbor along the trailing edge. Thus, the coincident filaments along the trailing edge cancel each other, and the Kutta condition is enforced.

This understanding of how the Kutta condition is enforced at the trailing edge can now be extended to explain the allocation of vorticity along the wing tip in the current work. First, it is necessary to note how the addition of supplementary vortex rings to represent the separated flow structure fundamentally changes the problem. By adding these elements without adding more collocation points at which the zero-normal-flow boundary condition can be enforced, the problem becomes underdetermined. If the wing tip is sharp and the Kutta condition can be assumed, as it can be at the trailing edge, this would present a convenient solution. The tip-vortex ring circulation magnitudes would be set to the same value as those of their respective bound neighbors; the circulation along the wing tip would be cancelled; and the problem would no longer be underdetermined.

However, wing tips are not necessarily sharp, and therefore it is expected that the boundary layer on the lower surface of the wing may remain attached for some portion of the full turn around the wing tip. In other words, some vorticity may remain bound to the tip. Indeed, this is the fundamental motivation for the augmentation used in the current work. Therefore, in order to solve the set of linear equations in equation 2.2 two new factors are introduced. The first is the critical vorticity value, Γ_{crit}, which defines the maximum amount of vorticity that may remain bound to each chordwise position along the wing tip. And, the second factor is the shed vorticity parameter, SVP, and is used to define the circulation of each free vortex ring in terms of the strength of its bound neighbor along the camber surface, as follows:

$$\Gamma_i' = SVP \times \Gamma_i$$

To relate this vorticity allocation to the enforcement of the Kutta condition along the wing tip, that case would simply correspond to an SVP value of 1. In that case, the strength of the free vortex ring would equal that of its bound neighbor, and the net vorticity along the wing tip would cancel. In the LOM, SVP has a value between 0 and 1. If the total vorticity at a given chordwise location along the tip does not exceed Γ_{crit} then no vorticity is shed and SVP equals 0. If Γ_{crit} is exceeded, then the balance of the vorticity is shed and feeds the free tip vortex at that chordwise location. In that scenario SVP equals a value between 0 and 1, such that the net circulation value along the wing tip would be equal to Γ_{crit}. In the current version of the LOM discussed in this paper Γ_{crit} is assumed to be a function only of tip geometry and therefore remains constant along the chord for the validations against the flat plate experiments conducted by DeVoria and Mohseni. It is important to note that the value of Γ_i changes with each iteration, as the location and strength of the free vortices change (see the following subsection). Therefore, SVP must be recalculated at each iteration, as follows:

$$SVP = \begin{cases} 0 & \Gamma_i \leq \Gamma_{crit} \\ 1 - \frac{\Gamma_{crit}}{\Gamma_i} & \Gamma_i > \Gamma_{crit} \end{cases} \tag{2.10}$$

The following subsection explains the second consequence of adding supplementary vortex rings to represent the separated shear layer and tip vortex: the program must now iterate to find a solution, because the free tip vortex positions are not known apriori.

2.2.2 Iterating to Find the Positions of the Tip Vortices

Generally speaking, it is possible for free lattice structures in a VLM to roll-up on themselves in ways that can make convergence difficult or impossible to achieve. The simple geometry of the free vortex filaments and the methods used to adjust their positions at each iteration were designed not only to reduce computation time, but also to restrict the repositioning of the tip-vortex filaments in a way that discouraged roll-up.

Just as for the camber surface itself, the tip vortex and separated shear layer are represented by a sheet of vortex rings, albeit free instead of bound. And, just as for a conventional VLM, the circulation strengths of all vortex filaments—bound and free—are calculated as those necessary to satisfy the zero-normal-flow boundary condition at the collocation points and the Kutta condition along the trailing edge. A conventional VLM depends on a known wing geometry to construct the AIC matrix, which describes the induced velocity contribution (normal to the panel) at each collocation point from each of the vortex filaments in the model. Therefore, the ultimate success of the LOM depends on its ability to accurately locate the free tip vortices, such that the geometry is fully defined and equation 2.2 can be solved. However, because the locations of these free filaments are not initially known, the model must begin with an estimated location and then iterate to find a solution. At each iteration, the tip-vortex position is adjusted to follow the local streamline, and the SVP values are recalculated at each chord-wise position based on how much vorticity the wing tip can support, using equation 2.10.

Because the separated flow structure at the wing tip is force-free, the tip vortex should follow the local streamline. Therefore, the model initiates the tip vortex at the leading-edge corner and then uses local velocities to determine each downstream position. To obtain these local velocities, a new matrix called the T matrix is calculated. This matrix, like the AIC and F matrices described above, expresses the velocity induced at a series of points by all of the vortex filaments in the model, and can be used to calculate these velocities when $\mathbf{\Gamma}$ is known.

$$[T]\mathbf{\Gamma} = \boldsymbol{V_{ind}} \tag{2.11}$$

In this case, these points are the series of free vortex positions, beginning with the corner representing the leading-edge / tip corner of the wing, that are one chordwise-lattice-position upstream of each free tip-vortex point. The velocities at these points are added to the free-stream velocity (equation 2.12) and are used to "steer" the tip vortex as it traverses the distance from one position to the next. This process of repositioning the tip vortices is done in two steps. First, the y and z-coordinates at each position are adjusted, based on the local velocity given by equation 2.12. And second, the x-coordinates are adjusted to maintain a particular orientation of the shear layer elements. This orientation is described in the following paragraph.

$$\boldsymbol{V} = \boldsymbol{V_{\infty}} + \boldsymbol{V_{ind}} \tag{2.12}$$

As illustrated in Figure 2.1 above, the vortex filaments that represent the shear layer are set at an angle to the y-z plane. This angle approximates the net of the outward flow from the wing tip and the free-stream velocity. Generally speaking, this angle was chosen to approximate the actual flow direction in the shear layer, because in a force-free wake the vortex filaments should parallel the local streamlines. Specifically, this angle was chosen to place these filaments in planes that contain a free-stream velocity vector and a line parallel to the y-axis. Such an angle matches the angle of the wing wake in the x-z plane and locates the downstream tip vortex in the plane of the wing wake, thus approximating the real flow. The action that occurs downstream of the wing in a real flow is that of the wake being rolled-up into the tip vortices, and there is, in fact, no distinction between the two, as there is in the LOM. Therefore, this configuration of the tip vortex and wing wake relative positions was an effort to approximate this flow.

Convergence of the model is defined as the configuration of the model when the maximum distance moved by all tip-vortex points from the previous iteration to the current iteration is less than a certain multiple of the average wing chord. A value of 0.02 was used in all analyses. For situations in which convergence proves challenging, the model is equipped with a damping factor chosen by the user. A value of 0.5 was used in all analyses. In order to maintain the same standards of convergence when this damping factor is used, the convergence criterion is proportionally tightened.

2.2.3 Steps of the LOM

The following steps are taken by the model:

1. The LOM is first run without free vortices and the lift is calculated. Based on the lift direction, the program determines which side of the wing is the suction side, and therefore the side of the wing on which the free tip vortices originate. For example, a positive lift would produce free tip vortices on the upper surface. Additionally, AIC and F matrices are calculated during this step and are used as the base matrices upon which the influence of the free tip vortex filaments are added in subsequent calculations. Re-using these base matrices at each iteration reduces computation time by approximately 80%, and is made possible by the fact that the bound vortex locations do not change from one iteration to the next.
2. The initial positions of the free tip vortices are guessed.
3. The LOM is run with the current tip-vortex positions; the Γ values are found; the T matrix is calculated to get "steering" velocities for the tip vortices; the tip vortices are repositioned; and, SVP values are recalculated.
4. Step (3) is repeated until convergence is achieved.
5. Once convergence is achieved, the LOM is run one last time with the latest tip-vortex positions; the Γ values are found; the F matrix is calculated; and, the forces and moments are calculated.

2.2.4 Determination of Γ_{crit}

In initial work, RANS CFD (FLUENT) data was used to determine Γ_{crit} for each chordwise position. The runs were made using an unswept wing with a NACA 4415 airfoil, an aspect ratio of 8, a flat tip geometry, at a Reynolds number of 3 million and a Mach number of 0.12. The Spallart-Almaras viscosity model was used. The x-location of initial shear layer separation along the tip (x_{sep}) was taken from the CFD output as the point along the wing tip at which span-wise shear stress changed from inboard to outboard, as shown in Figure 2.2. For the unswept wings studied thus far, the thinking was that this point corresponded to the initiation of reversed flow (i.e. outboard flow) associated with flow separation, and therefore could be taken as the origin of the main tip vortex. Then, the LOM was run at the same α, but without free tip vortices, meaning it functioned as a conventional VLM. At this α, the Γ value from the tip lattice most nearly located at x_{sep} represented the net vorticity at that location, and was therefore taken as Γ_{crit}. These Γ_{crit} values were then used in the low-order model as constants for a given wing-tip geometry, regardless of angle of attack or sideslip angle.

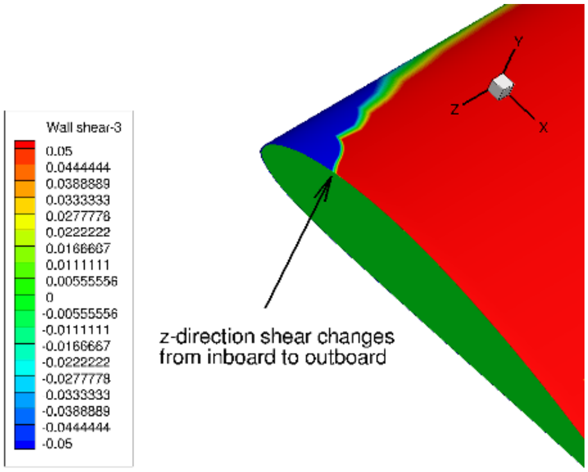

Figure 2.2: From CFD: spanwise shear stress indicating the position of the most upstream outboard flow.

Results showed that this method provided a good first order approximation Γ_{crit}. However, Γ_{crit} was ultimately chosen to be that value which best matched the lift curve at angles of attack from 0° to 10°.

2.3 Capabilities of the Model

The LOM has the following capabilities.

1) It can function as a conventional VLM without the influence of tip vortices (left side of Figure 2.3) or with free tip vortices (right side of Figure 2.3). In the first case, the tip vortices are still shown, but have circulation values of zero and therefore have no effect. The LOM has been successfully validated against the public domain vortex lattice code known as AVL for a range of aspect ratios, angles of attack, sideslip angles and lattice densities.

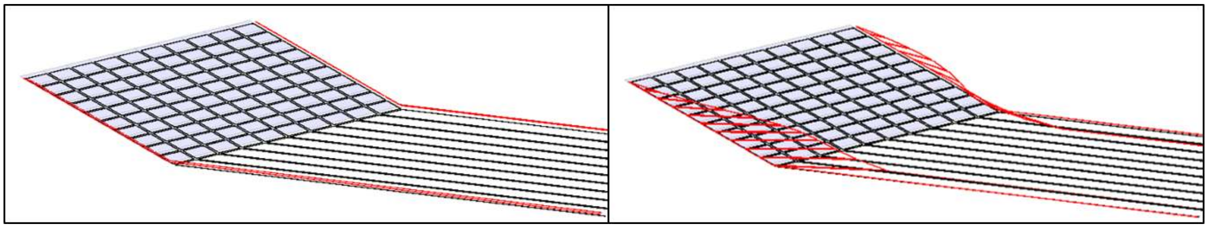

Figure 2.3: LOM can operate as a conventional VLM (left) or with free tip vortices (right). Black: vortex filaments typical of conventional VLM; red: supplementary free shear layer and tip-vortex filaments. light blue: camber surface; $\AE = 1$, $\alpha = 15°$, $\beta = 0°$, $\Gamma_{crit} = 0$.

2) The tip-vortex origin may be located where vorticity is first shed from the wing tip (left side of Figure 2.4) or assigned a particular chordwise position, such as the leading edge (right side of Figure 2.4). In the latter case, the tip vortex is allowed to follow the local velocity, even where it has a circulation value of zero near the leading edge. In the current work, the tip-vortex origin is assigned to the leading-edge position, because convergence proved difficult when the origin was allowed to change position from one iteration to the next.

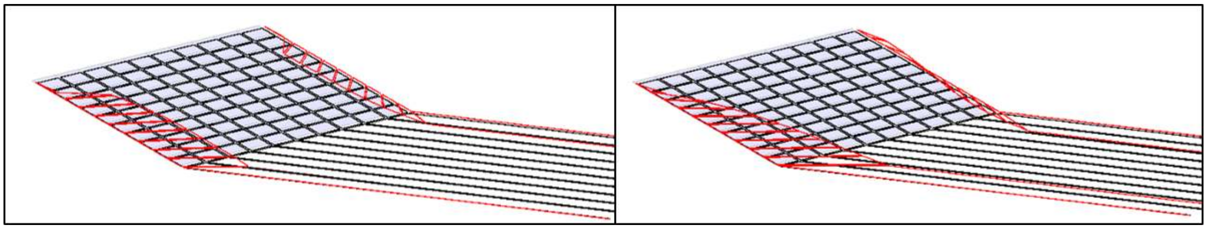

Figure 2.4: The tip-vortex origin may be located where vorticity is first shed from the wing tip (left) or forced to separate at a point, such as the leading edge (right); $\AE = 1$, $\alpha = 15°$, $\beta = 0°$, $\Gamma_{crit} = 0.073$.

2.4 Inputs

The LOM requires the following inputs:

1. **Airfoil**. The camber surface may be flat, or defined by any airfoil shape.
2. $\boldsymbol{\AE}$, aspect ratio
3. $\boldsymbol{\alpha}$, angle of attack
4. $\boldsymbol{\beta}$, sideslip angle
5. **M**, number of chordwise lattices.
6. **Lattice Aspect Ratio**. Given the overall wing $\AE$, this defines the number of spanwise lattices, N.
7. $\boldsymbol{\Gamma_{crit}}$, This is the critical vorticity value above which vorticity is shed to feed the free vortex. This value can be specified uniquely for each chordwise position, however in this paper it is taken as a constant along the chord.
8. **Tip Vortices**. Choose to include free tip vortices or to operate as a conventional VLM, without free tip vortices.

9. **Tip-Vortex Origin Point**. Choose if the tip vortices are free to originate at any location, based on whether vorticity is being shed, or forced to originate at a particular chordwise position. The tip vortex is forced to separate at the leading edge in the current work.

10. **Tip-Vortex Origin Surface**. Choose if the tip vortices will originate from the camber surface or from the wing surface (only applicable when using a specified airfoil). The camber surface was chosen in the current work.

11. **Damping factor**. This value is between 0 and 1 and specifies how much of the full change in tip-vortex locations will be used by the LOM at each iteration. 0.5 was used in the current work.

12. **Convergence Criterion Factor**. This factor sets the convergence criterion as this multiple of the average chord length. 0.02 was used in the current work. This factor is proportionally reduced according to the damping factor.

13. **Iteration Limit**. This sets the number of iterations at which the LOM terminates and declares that convergence has failed. Typically, a value of 50 was used.

14. **Core Size Factor**. This factor defines the core size as a multiple of the average lattice width (spanwise dimension). The core size is set as a critical radius around a vortex filament, within which the velocity magnitude induced at a given point is set to zero. 10^{-5} was used in the current work. It serves as a protection against spurious results near the vortex core where velocity magnitudes become infinite. In actual flow, the core is considered to be dominated by viscosity, and therefore approximates solid-body rotation, with the velocity linearly dropping to zero at the center.

Chapter 3

Results

The results presented in this paper are validated against five sources.

1) Tip-vortex positions at the trailing edge are compared to experimental work by Engel [3]. Using helium bubble flow visualization Engel studied the flow around the tip of a wing with a NACA 0012 airfoil and an Æ of 3 at Reynolds numbers of 130,000 and 335,000.

2) Tip-vortex positions at mid-chord and the trailing edge are compared to an empirically-based model by Ramaprian [33]. He studied the tip-vortex locations in the near wake of rectangular wings and developed the following approximations of the tip-vortex coordinates, where the origin lies at the leading-edge / wing-tip corner.

$$y_0^* = 0.09(x_v^*)^{0.75} \tag{3.1}$$

$$z_0^* = 0.09(x_v^*)^{0.5} \tag{3.2}$$

where

$$x_0^* = \frac{x_0}{L}$$

$$y_0^* = \frac{y_0}{L}$$

$$z_0^* = \frac{z_0}{L}$$

and

$$L = \frac{cC_L}{2}$$

3) Tip-vortex positions at mid-chord and the trailing edge are compared to CFD results from work performed at NCSU. The runs were made using an unswept wing with a NACA 4415 airfoil, an aspect ratio of 8, a flat tip geometry, at a Reynolds number of 3 million and a Mach number of 0.12. The Spallart-Almaras viscosity model was used. The tip-vortex location was identified as the point of greatest x-vorticity.

4) Lift is compared to CFD results from work performed at NCSU. The runs were made using an unswept wing with a NACA 0012 airfoil, aspect ratios of 1 and 3, a flat tip geometry, at a Reynolds number of 80,000. The Spallart-Almaras viscosity model was used.

5) Tip-vortex positions, forces and moments are compared to experimental work performed by DeVoria and Mohseni [30]. They measured loads and used S-DPIV to capture the flow around LAR flat plate wings and across a large range of angles of attack and sideslip angles, with aspect ratios ranging from 0.75 to 3 at a Reynolds number of 80,000.

3.1 Tip-Vortex Position

Figure 3.1 presents a comparison of tip-vortex positions predicted by the LOM to the results of Engel and Ramaprian's model. The results are of the left wing tip-vortex positions at the trailing edge of a wing with a NACA 0012 airfoil, for Æ of 3, α of 7.5° and no sideslip. Engel's experiments were conducted at a Reynolds number of 335,000. As an additional element of analysis, three different values of Γ_{crit} were used to illustrate the effect on tip-vortex positions in the LOM. There is a clear inboard movement with an increase in Γ_{crit}, which is consistent with results from the "Vortex Flow Experiment 2" [29] discussed in Chapter 1.

The wing with the best tip-vortex location agreement is that with a Γ_{crit} value of 0. However, it should be noted that force and moment agreement for the CFD analyses performed at NCSU on LAR wings with NACA 0012 indicate that a thicker wing should be able to support some non-zero value of vorticity along the wing tip. These results are included below in the lift validation subsection. As discussed in Chapter 1, thickness effects present a particular challenge in accurately locating the tip-vortices. The wing is modeled as having zero thickness in the LOM, so the orientations of streamlines in this region necessarily differ from those of actual streamlines that follow the surface of a profiled wing of non-zero thickness. Overall, the tip-vortex location agreement is quite good, and the inboard movement of the tip vortices is correctly modeled, even if the particular Γ_{crit} value does not necessarily correspond to the correct position.

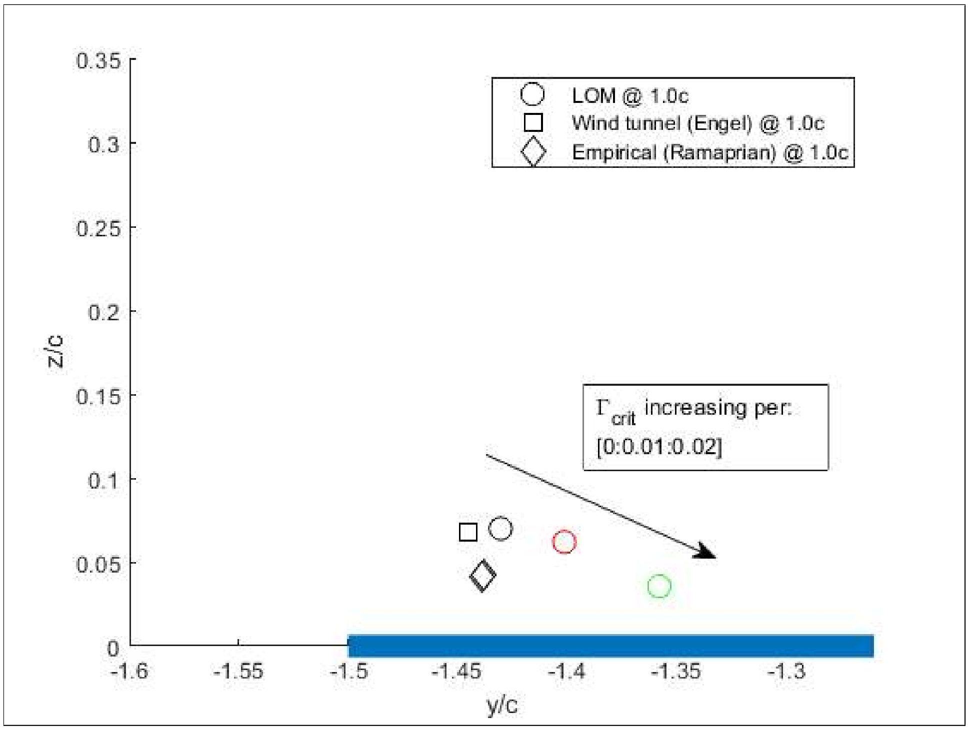

Figure 3.1: Left wing-tip vortex positions for wing with NACA 0012 airfoil, Æ of 3, α of 7.5°, β of 0°, at a Reynolds number of 335,000 in Engel's work [3]; 10 chordwise lattices and 30 spanwise lattices used. Wing represented by blue line.

As a point of comparison, Figure 3.2 presents a comparison of left wing-tip vortex positions for a higher-Æ wing, again without sideslip. The positions were taken at the mid-chord and trailing edge of a wing with a NACA 4415 airfoil, Æ of 8, α of 12°, at a Reynolds number of 3×10^6 in the CFD work performed at NCSU. As in the previous example, three different values of Γ_{crit} were used to illustrate the effect on tip-vortex positions. And, again, there is a clear inboard movement—at mid-chord and the trailing edge—as Γ_{crit} increases. The upward trend when moving from mid-chord to the trailing edge from Ramaprian's work is successfully captured by the LOM. However, the predicted locations are well inboard of those of the CFD and empirical models.

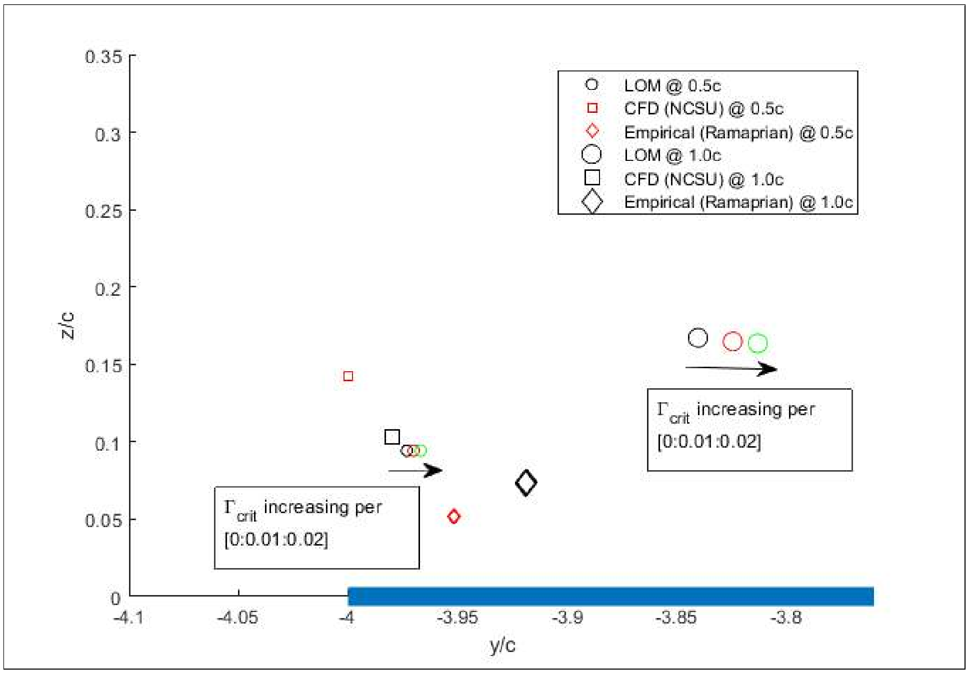

Figure 3.2: Left wing-tip vortex positions for wing with NACA 4415 airfoil, Æ of 8, α of 12°, β of 0°, at a Reynolds number of 3×10^6 in CFD work performed at NCSU; 10 chordwise lattices and 80 spanwise lattices used. Wing represented by blue line.

3.2 Lift Generation

Figure 3.3 presents plots of forces and moments versus α, without sideslip for a flat plate of Æ of 1. Results include those from the LOM, both without free vortices and with free vortices at multiple values of Γ_{crit}, as well as experimental flat plate results from DeVoria and Mohseni and CFD work from NCSU. As a point of comparison for the LOM without free vortices, lift coefficients predicted by the Helmbold equation (see below) are also provided. This equation is commonly used to modify the lift-curve slope for LAR wings below an Æ of 4 at low angles of attack.

$$a = \frac{a_0}{\sqrt{1 + \frac{a_0}{(\pi \text{Æ})^2}} + \frac{a_0}{(\pi \text{Æ})}} \tag{3.3}$$

where a_0 is the airfoil lift-curve slope of $2\pi/rad$ and a is the modified lift-curve slope.

There are multiple aspects of these results that are worth noting. First, the LOM model without free tip vortices matches quite well with the Helmbold Equation results, which provides further validation of the LOM operating without free tip vortices, beyond that carried out using AVL. Second, when free tip vortices are included in the LOM there is a clear increase in lift and drag beyond what is predicted without them, which is consistent with the expected vortex lift and vortex drag associated with LAR wings. Third, an ability to “throttle” the forces and moments based on how much vorticity is supported by the wing-tip edge has been demonstrated, which meets one of the main objectives of this research effort. It is evident that with a Γ_{crit} value of 0, it is possible to achieve a fairly good fit of the flat plate lift curve. And, the Γ_{crit} value that best corresponds to the lift curve of the thicker-profiled wing with NACA 0012 airfoil, is higher than for the flat plate. Given that the NACA 0012 wing is thicker (12% versus 4.2% for the flat plate), one would expect the tip to be able to support more vorticity and thus produce less vortex lift.

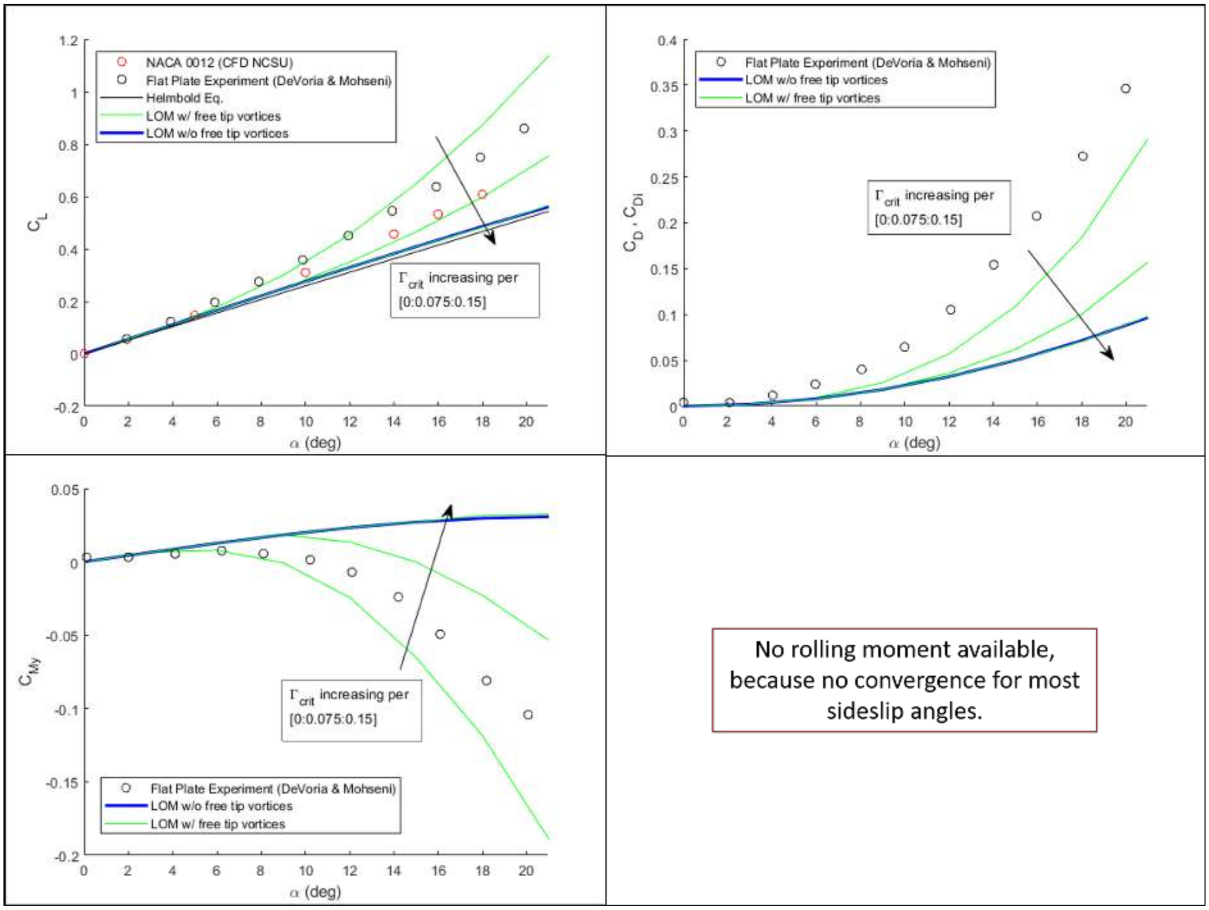

Figure 3.3: Forces and moments with increasing Γ_{crit}, demonstrating that predictions approach and then coincide with conventional VLM results as Γ_{crit} increases; Æ $= 1$, 10 chordwise lattices, 10 spanwise lattices. Rolling-moment results omitted, due to failure of the LOM to converge in sideslip with the planar shear layer geometry.

3.2.1 Determining the Optimal Number of Chordwise and Spanwise Lattices

Before proceeding further, a study to determine a sufficient number of lattices is presented using lift, drag and pitching moment for a wing with an Æ of 1. Computation time increases nonlinearly with the total number of lattices, therefore this study was conducted to determine the minimum number of lattices required to achieve sufficiently accurate results, while minimizing computation time. Figure 3.4 presents the forces and moments predicted by the LOM for a flat plate of Æ $= 1$ at a single value of Γ_{crit}, but with multiple values of the number of chordwise lattices, M. For all runs, the lattice Æ is kept at 1, meaning that the number of spanwise lattices, N, is equal to M.

First, focusing on the conventional VLM cases (blue plots), it is evident that a sufficient degree of convergence is achieved by using 10 chordwise lattices. Not only is there little difference in forces and moments as 10 chordwise lattices is approached, but there is close agreement with the lift predicted by the Helmbold equation. Second, focusing on the LOM cases (green plots) there is close agreement up to an angle of attack of 10°. However, beyond this point, there appears to be some degree of divergence as the number of chordwise lattices increases. This is of some concern, and studies were conducted to investigate the possible causes. However, no conclusions have been made as of this writing, and further investigations will be required in future work.

It is worth mentioning that in earlier versions of the LOM, the shear layer filaments had an alternate orientation that did not cause this divergence. In those versions, these filaments were located in the same planes as their respective spanwise bound filaments; and in those cases this apparent divergence was not present. However, the reason why the orientation of the shear layer filaments was changed to that of the current LOM was that the earlier orientation created an erroneous suction peak at the leading-edge / wing-tip corner, which likely contributed to what was very poor prediction of pitching and rolling moments. As will be presented in the following sections, there has been some improvement in prediction of these moments with the newer shear layer filament orientations.

The conclusion as of this writing is that 10 chordwise lattices is sufficient and appropriate for the LOM for the results presented in this paper. This represents a compromise that recognizes the greater fidelity that more chordwise lattices offers for LAR wings, generally, while also recognizing that 10 chordwise lattices for the LOM predicts forces and moments that are still quite close to that predicted by the LOM with fewer chordwise lattices.

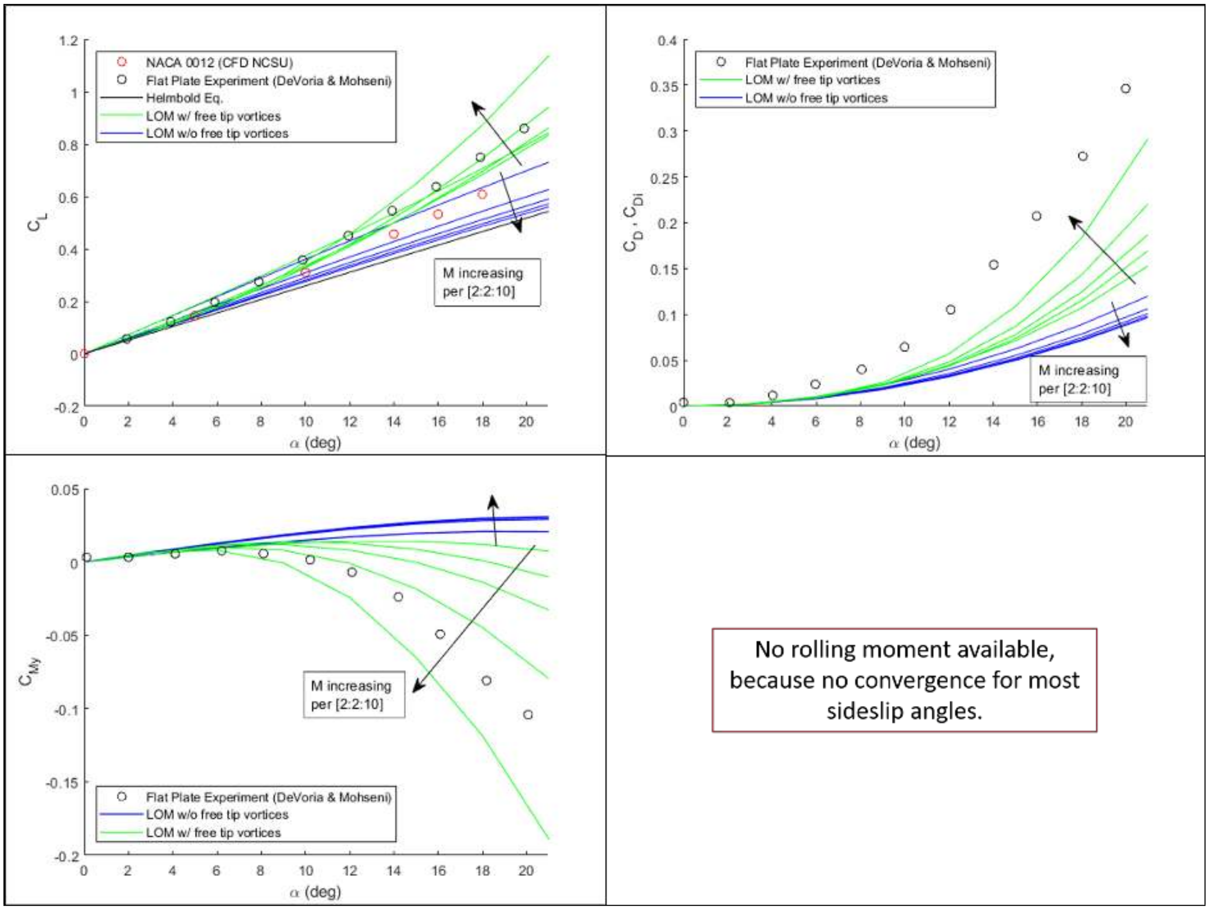

Figure 3.4: Forces and moments predicted by the LOM with multiple values of the number of chordwise lattices, M; $\text{Æ} = 1$, $\Gamma_{crit} = 0$. Rolling-moment results omitted, due to failure of the LOM to converge in sideslip with the planar shear layer geometry.

With the necessary number of chordwise lattices established, a second study was conducted to study the sensitivity of the results to the lattice Æ, again using force and moment plots (Figure 3.5). A higher lattice Æ would allow for fewer lattices, and therefore a reduction in computation time. However, this would likely reduce accuracy. The results showed a satisfactory level of convergence as the lattice Æ decreases and approaches 1, and it should be noted that for some cases the code did not converge for a lattice Æ less than 1. Based on these results, the lattice Æ is kept at or just above a value of 1 whenever possible throughout the analyses discussed in the remainder of this paper.

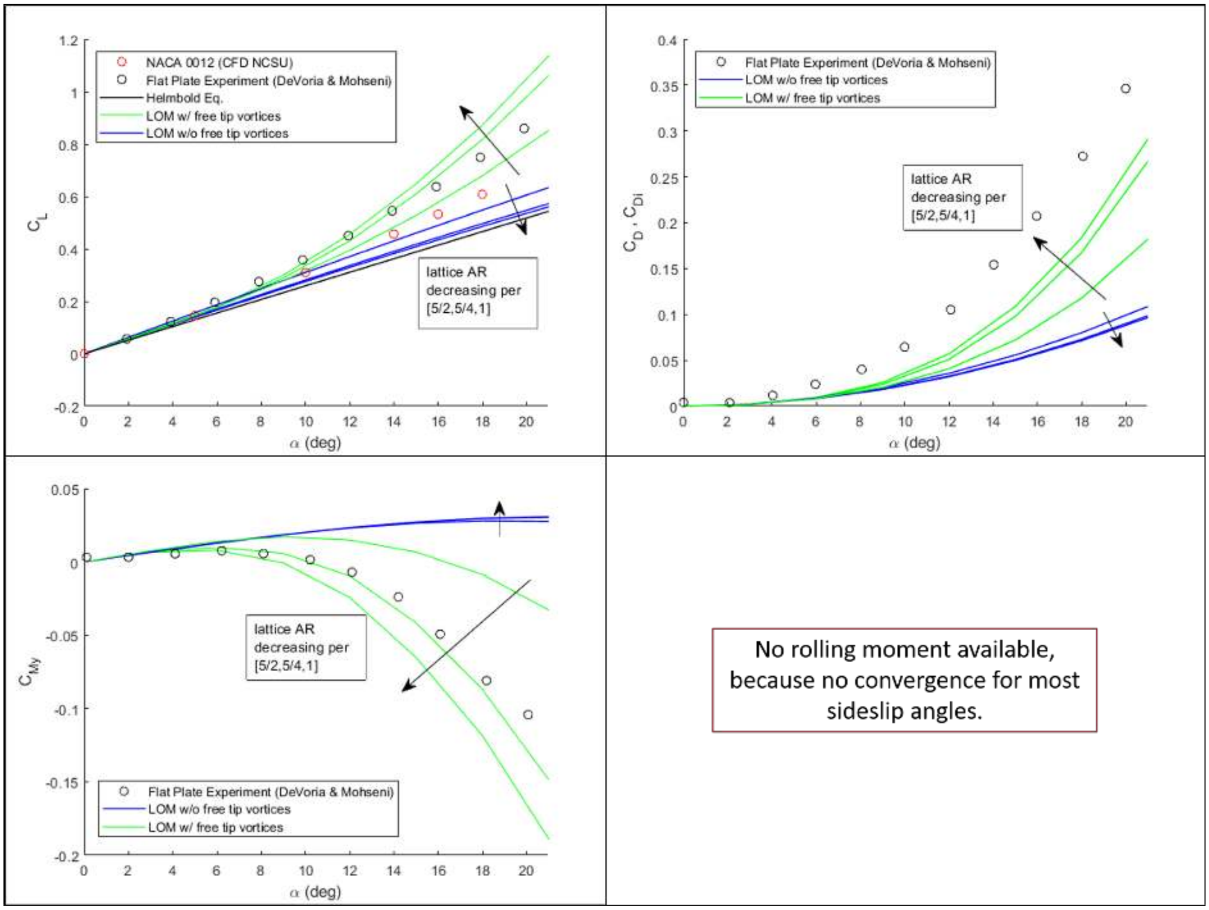

Figure 3.5: Forces and moments predicted by the LOM with multiple values of the number of spanwise lattices, N, as defined by the lattice Æ; M = 10, Æ = 1, $\Gamma_{crit} = 0$. Rolling-moment results omitted, due to failure of the LOM to converge in sideslip with the planar shear layer geometry.

3.2.2 Lift Distribution Studies: Verifying the Production of Vortex Lift

With the optimal number of chordwise and spanwise lattices established, the lift validation continues, and the discussion returns to vortex lift. As demonstrated above, the LOM is able to "throttle" lift by controlling Γ_{crit} and appears to capture the characteristic nonlinear lift curve associated with vortex lift, as discussed in Chapter 1. To investigate whether this is indeed the nature of this additional lift, multiple lift distributions were examined. First, Figure 3.6 presents spanwise lift distributions that are consistent with the characteristic lift distributions associated with fully-attached flow (left) and the suction peaks associated with each free tip vortex (right), as illustrated in Figure 3.9 of Chapter 1. Also evident on the right image is a portion of the familiar, rounded lift distribution that peaks toward mid-span and is a result of fully-attached flow, indicating that both types of lift are generated.

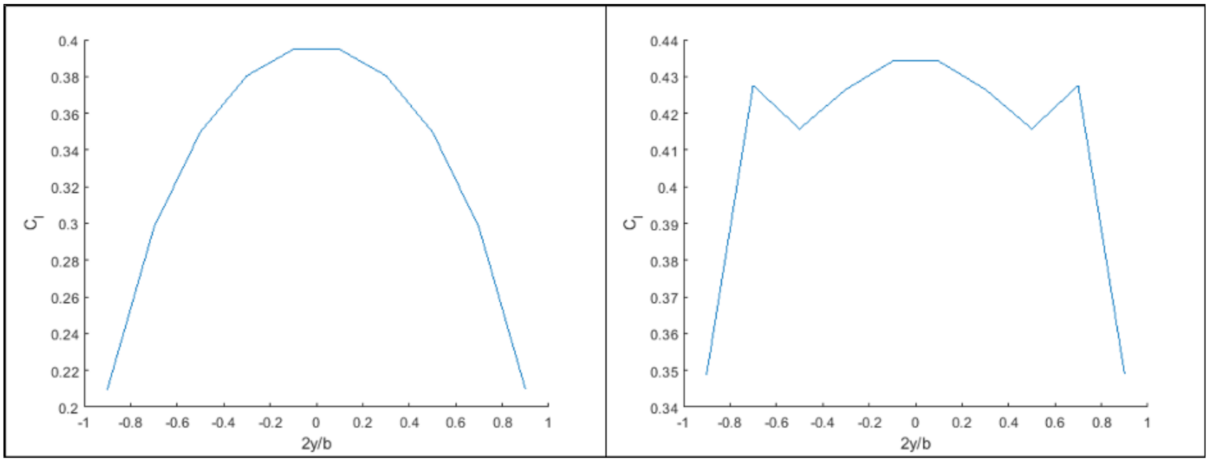

Figure 3.6: Spanwise lift distributions for an uncambered wing, $AR = 1$, $\alpha = 12°$, $\beta = 0°$; Left: Conventional VLM; Right: LOM with free tip vortices, $\Gamma_{crit} = 0$; 10 chordwise lattices, 10 spanwise lattices.

Next, the same plot was made for multiple aspect ratios to confirm that lift increases with AR and that the vortex lift near the wing tips is less significant for higher aspect ratios. As presented in Figure 3.7, as AR increases, the vortex lift peaks are pushed farther towards the tips and comprise less of the total overall lift. The highest AR wing ($AR = 1.5$) has a clear "linear" lift signature towards mid-span, while the lowest AR wing ($AR = 0.5$) has no clear "linear" lift signature and appears to be dominated by vortex lift. Additionally, as AR increases, the total lift increases substantially, as expected.

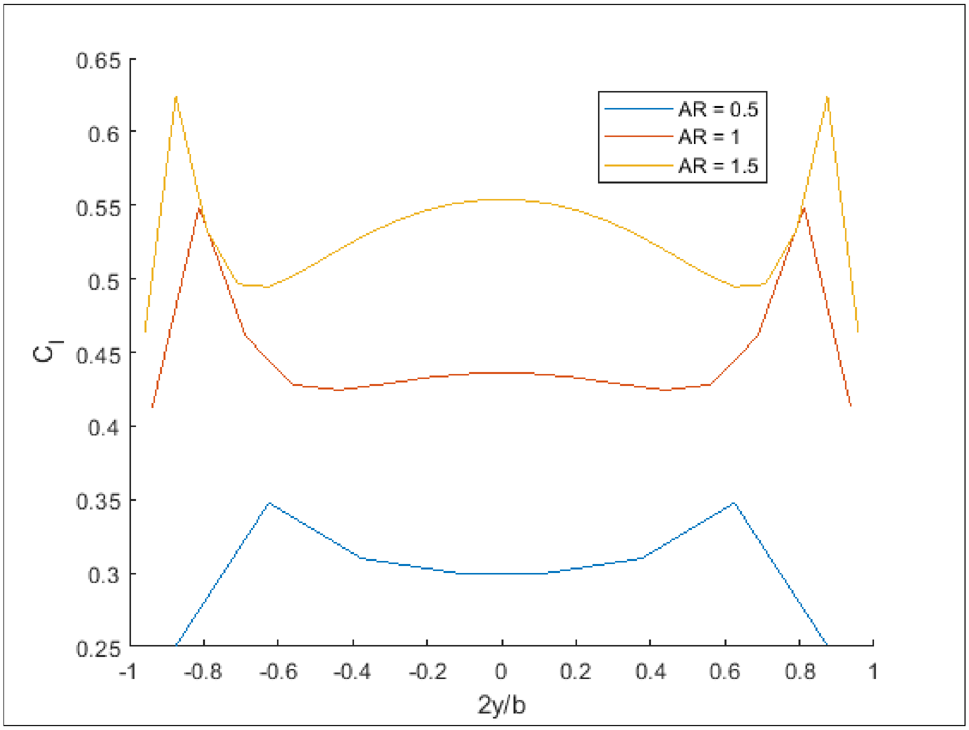

Figure 3.7: Spanwise lift distributions from LOM for uncambered wings at multiple $\mathcal{R}$s, Γ_{crit} = 0, $\alpha = 12°$, $\beta = 0°$, 10 chordwise panels, lattice $\mathcal{R} = 0.625$.

As demonstrated above, the total lift can be “throttled” by controlling the maximum allowable bound vorticity along the wing tips. In this regard, the characteristic suction peaks associated with vortex lift ought to be more pronounced as Γ_{crit} decreases, and Figure 3.11 demonstrates this trend successfully. In the figure, spanwise lift distributions of an uncambered wing at multiple values of Γ_{crit} are presented, with the plot of Figure 3.3 included to locate each scenario along its respective lift curve. The wing has an $\mathcal{R}$ of 1; α is 18°; and there is no sideslip. At the lowest value of Γ_{crit} the total lift is greatest and the lift distribution demonstrates the clearest signature of vortex lift near each wing tip, with the trend diminishing as Γ_{crit} increases. At the highest value of Γ_{crit} the lift is lowest and the lift distribution shape is consistent with “linear” lift that would be expected from fully-attached flow. And, in fact, that is precisely what it is. At a sufficiently large Γ_{crit}, the wing tips are capable of supporting enough vorticity that no vorticity is shed and no vortex lift is created. All of the lift in this scenario arises from fully-attached flow. All of these observations are consistent with the associated points on their respective lift curves: (i) the total lift increases with decreasing Γ_{crit}, and the lift curve approaches—and, eventually coincides with—the "linear" lift curve as Γ_{crit} increases.

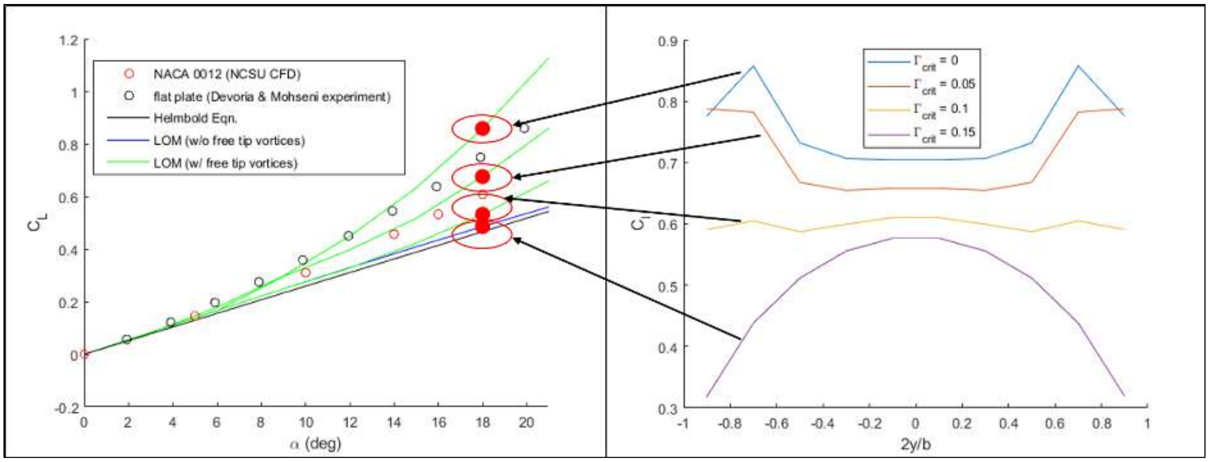

Figure 3.8: Spanwise lift distributions for an uncambered wing at multiple Γ_{crit} values, $Æ = 1$, $\alpha = 18°$, $\beta = 0°$, 10 chordwise panels, 10 spanwise panels.

It is also worth examining both the spanwise and chordwise distributions to better understand how the chordwise lift distributions contribute to these spanwise lift distributions presented thus far (see Figure 3.10). The purpose of these plots is to demonstrate their consistency with the "linear" and "nonlinear" lift distributions from the experimental and CFD work presented in Chapter 1. Figure 3.9 (also included in Chapter 1) is included first as a reminder of a typical pressure distribution on the suction side of an LAR wing with an angle of attack of 18° and no sideslip. The suction zone along the leading edge associated with "linear" lift is clearly evident, and the vortex lift along the side edges is increasingly evident as Γ_{crit} decreases. These distributions help confirm that suction zones associated with the tip vortices exist in the areas expected and that vortex lift is responsible for the additional lift predicted by the LOM when free tip vortices are included.

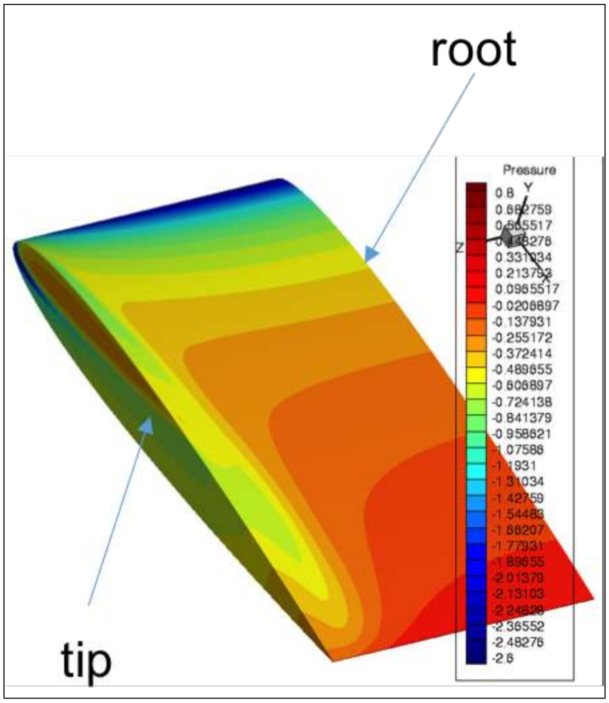

Figure 3.9: CFD results: pressure distribution on suction side of wing with NACA 0012 airfoil, $\alpha = 18°$, $\AE = 1$, Re = 80,000, demonstrating suction near tip due to free tip vortex and suction along leading edge associated with attached flow.

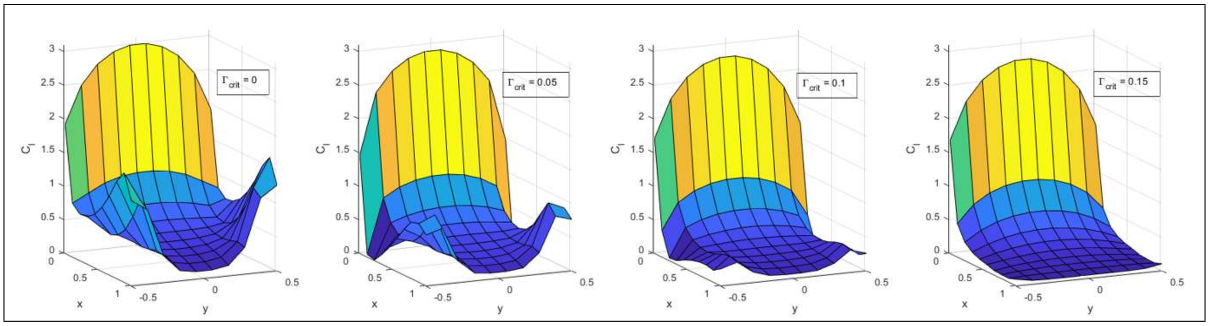

Figure 3.10: Spanwise and chordwise lift distributions from the LOM for an uncambered wing, with Γ_{crit} increasing from left to right, $\AE = 1$, $\alpha = 18°$, $\beta = 0°$, 10 chordwise panels, 10 spanwise panels.

The effect of angle of attack on the lift distribution is presented in Figure 3.11 to illustrate that vortex lift is responsible for the increasing supplementary lift that is created as α increases. Lift distributions are plotted for three angles of attack, 6°, 12° and 18°, and Γ_{crit} is held at zero for all plots. A lift curve is included (left side) to locate each scenario along its respective point on the lift curve. The lift increment for each 6° jump in angle of attack should increase nonlinearly, and that is evident in the plot, with a slightly greater jump in lift over the higher α increment. Furthermore, one would expect vortex lift to play a larger role as α increases, where the nonlinear lift deviation from "linear" lift is greatest. And, that is evident as well. At an α of 6°, there is very little indication of suction peaks near each wing tip, while at 18°, the suction peaks are very evident. This is consistent with the idea that the greater deviation from "linear" lift at higher angles of attack presented in Figure 3.3 is a consequence of vortex lift.

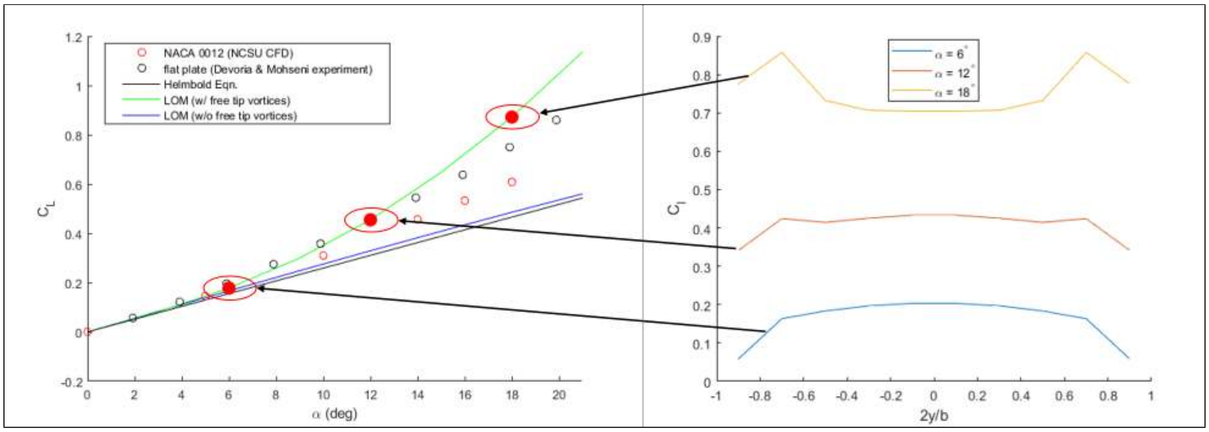

Figure 3.11: Spanwise lift distributions for an uncambered wing at multiple α values, $Æ = 1$, $\Gamma_{crit} = 0$, $\beta = 0°$.

A final look at lift distributions is presented to examine the effects of sideslip. For multiple β angles, the spanwise lift distributions are presented in Figure 3.12, and the distribution over the wing in both the spanwise and chordwise directions is presented in Figure 3.13. The spanwise distribution shows that the lift contribution along the upstream side of the wing clearly increases with sideslip, with a smaller, but significant decrease in lift along the downstream side. The chordwise lift distribution shows that this additional suction is occurring along the upstream wing tip, suggesting that vortex lift is at work. It is important to note that in other cases, when Γ_{crit} is non-zero, some flow is modeled as attached in the LOM as the wing tip acts, in part, as a "leading edge." Therefore, the lift along the upstream wing tip may be a combination of "linear" and "nonlinear" lift. This distribution demonstrates how a negative sideslip produces a negative rolling moment, as confirmed by the results for the curved shear layer geometry presented in Appendix A.

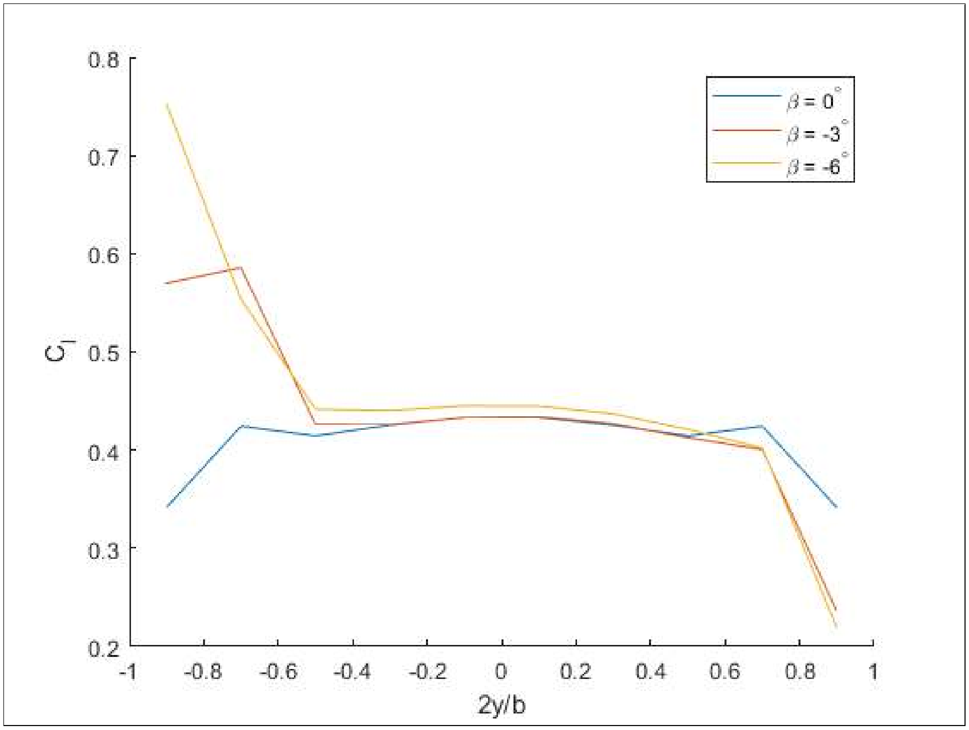

Figure 3.12: Spanwise lift distributions for an uncambered wing at multiple β values, $AR = 1$, $\Gamma_{crit} = 0$, $\alpha = 12°$.

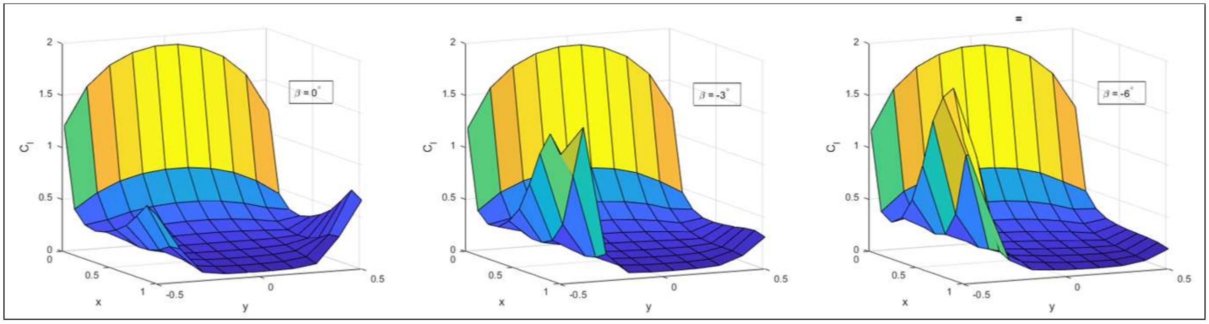

Figure 3.13: Spanwise and chordwise lift distributions for an uncambered wing with sideslip increasing from left to right, $Æ = 1$, $\Gamma_{crit} = 0$, $\alpha = 12°$.

3.3 Validation: Lift

To investigate the ability of the LOM to predict forces and moments, the value of Γ_{crit} was adjusted to match the lift curve of the lowest-aspect-ratio wing investigated by DeVoria and Mohseni: $Æ = 0.75$. The model was applied to increasingly higher $Æ$ values, keeping the value of Γ_{crit} held at that same value throughout. The reasoning behind this is that Γ_{crit} should primarily be a function of wing-tip geometry, and therefore should not change as $Æ$ changes. This value of Γ_{crit} was also used in the validations of drag, pitching moment and rolling moment that follow in the next sections. As discussed in Chapter 1, more focus was placed on α values below 10° in matching the lift curve, where leading-edge flow tends to be attached (or reattached).

Figure 3.14 presents fairly good agreement for all but the highest $Æ$ value of 3. In this latter case, the predicted lift is lower than the actual lift. Generally speaking the lift agreement is promising. And, because “linear” lift is predicted well by the LOM, any discrepancies should be attributable to differences in “nonlinear” lift. In this regard, it shows that the magnitude of the predicted vortex lift matches the actual vortex lift fairly well. Note that the best-fit value of Γ_{crit} is zero, which would be consistent with a thin wing such as the 4.2%-thick plate used by DeVoria and Mohseni. This is also consistent with the 12%-thick wing used in the CFD analyses, which produces less lift beyond “linear” lift and which would require a higher value of Γ_{crit}.

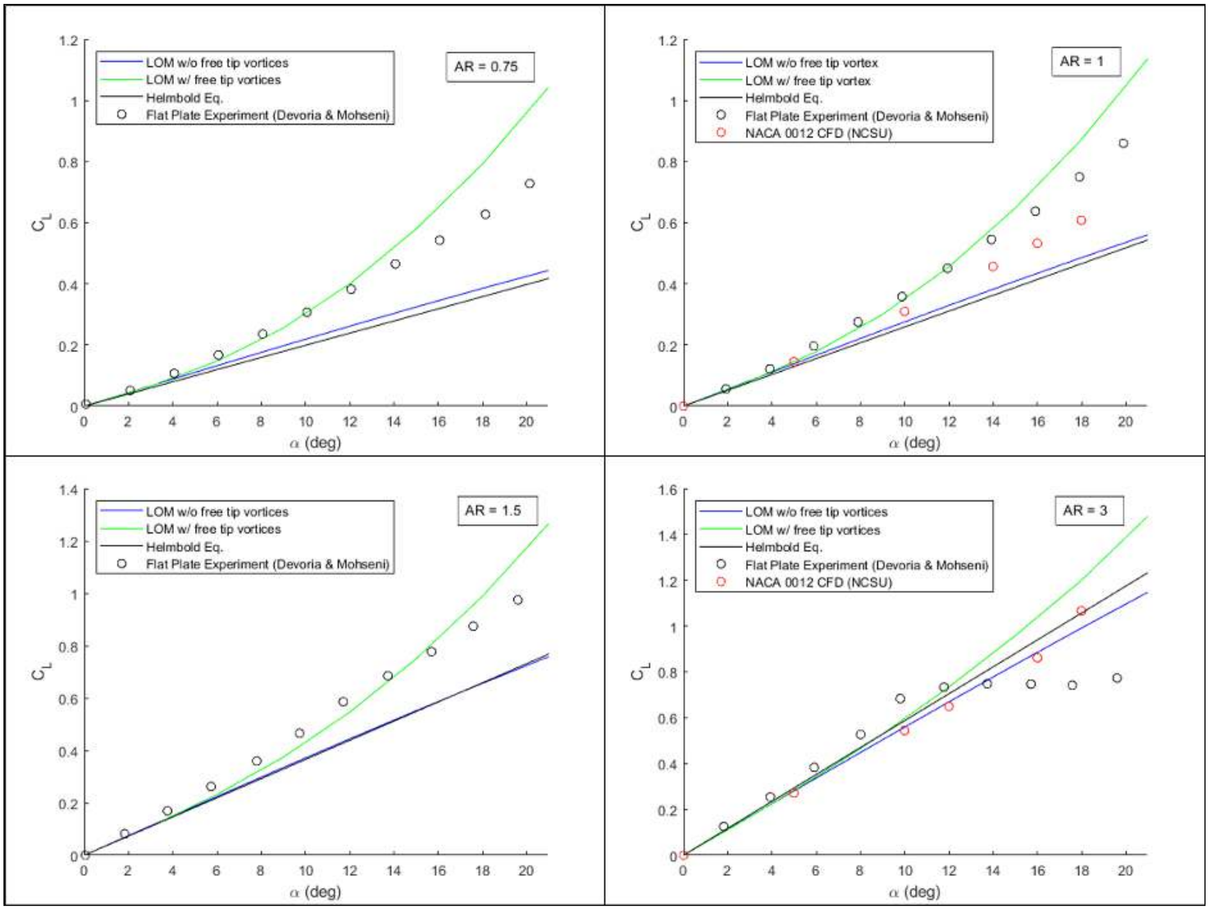

Figure 3.14: C_L versus α, $\Gamma_{crit} = 0$, no sideslip, Æ = 0.75, 1, 1.5 and 3.

3.4 Validation: Drag

Drag is notoriously difficult to predict for inviscid models, primarily because a potential flow model can only predict induced drag, which comprises only a portion of the total drag. This is particularly true for LAR wings, that involve complex, separated three-dimensional flows and coupled interactions between those flows. Considering this challenging aspect of drag, Figure 3.15 demonstrates fairly good agreement in drag trends for each Æ. As α increases, the discrepancies in drag grow. This is consistent with the increasing production of pressure drag that would result at higher angles of attack at which greater flow separation should occur, and the inherent inability of the inviscid LOM to capture pressure drag.

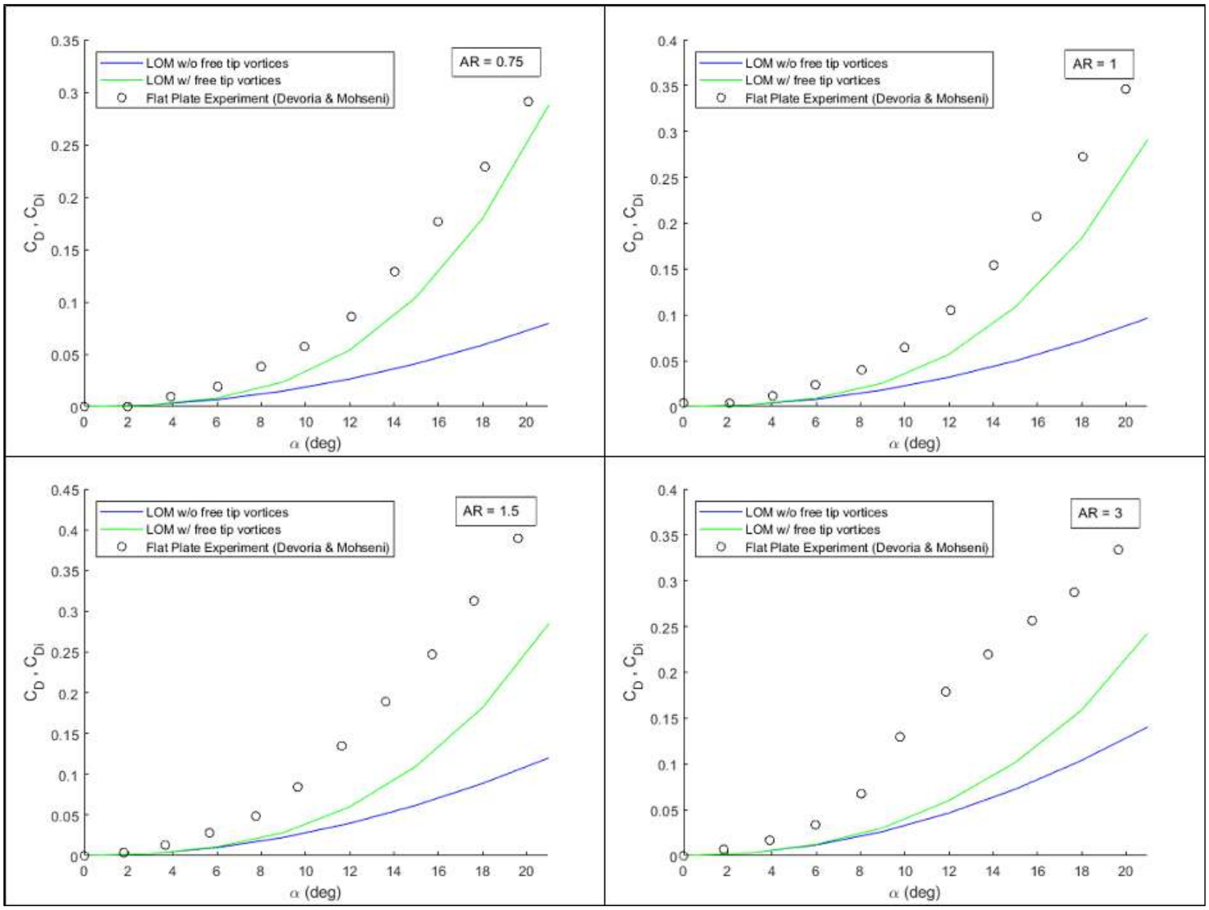

Figure 3.15: C_D / C_{Di} versus α, $\Gamma_{crit} = 0$, no sideslip, Æ $= 0.75$, 1, 1.5 and 3.

It is important to make a distinction between the separated vortical flows that the LOM is designed to capture along the wing tips and the flow around bluff bodies, which separates and does not reattach. DeVoria and Mohseni make the distinction that separated leading-edge flow that fails to reattach is considered “massively separated.” Where it separates but then reattaches, such as it does in the case of LAR wings for which downwash from the wing-tip vortices leads to reattachment of the separated leading-edge flow , it is referred to as “reattached flow.” Not only does the LOM lack the ability to capture the effects of this massively separated flow, but one of the main distinctions between the two types of flows is that massively separated flows are generally characterized by significant viscous dissipation, while shear layers that roll up, in the case of wing-tip vortices, or leading-edge separated flows that reattach, involve less viscous dissipation. This basic distinction of separated flow serves to explain the greater discrepancies in drag that occur for the highest aspect ratios. As explained by DeVoria and Mohseni, the leading-edge flow reattachment that occurs due to the downwash of the wing-tip vortices begins to diminish as aspect ratio increases. This means that more massively separated flow, and therefore more pressure drag, would occur with increasing $\mathcal{R}$. This finding helps to further define the window of best performance of the LOM as limited to LAR wings of $\mathcal{R}$ less than 3.

3.5 Validation: Pitching Moment

Figure 3.16 presents pitching-moment predictions, which show fairly good agreement with experimental results. It is evident from the negative pitching moments from the experiment at higher angles of attack that the center of normal force loading must be more aft than the loading produced by a conventional VLM. This should not be surprising, because it is known that the sharp leading-edge suction peak produced by a conventional VLM (and the LOM) over-predicts the strength of the true suction peak and places it too far forward, particularly as angle of attack increases. This lack of a leading-edge suction peak in the actual flow is confirmed by DeVoria and Mohseni in a plot of chordwise loading—in the form of spanwise vorticity, which shows a soft peak in loading near mid-chord, as opposed to the leading edge. As angle of attack increases, particularly beyond the range in which tip-vortex downwash reattaches the separated leading-edge flow, there would be very little lift generation near the leading edge, thus producing a pitching moment much more negative than that predicted by a conventional VLM. Considering that the pitching-moment prediction of the LOM shows fairly close agreement, despite its large leading-edge suction peak, this shows a significant ability of the LOM to capture vortex lift and its distribution.

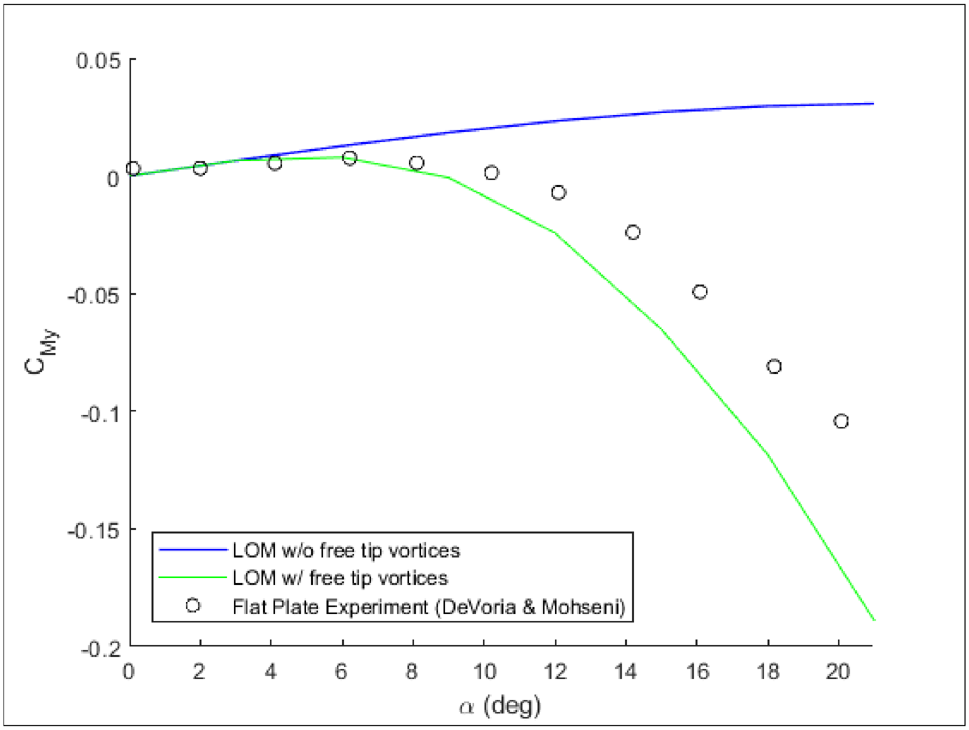

Figure 3.16: C_{My} versus α, $\Gamma_{crit} = 0$, no sideslip, $\text{Æ} = 1$.

3.5.1 Rolling Moment

The LOM failed to consistently converge for most configurations involving sideslip, and numerous variations on the model were tried to explore what might drive it to convergence. The damping factor, convergence criterion, point of free tip-vortex origin (location of first vorticity shedding instead of the leading edge, as well as the wing surface instead of the camber surface) were all varied. Another variation was the use of local velocities calculated along the wing tip to "steer" the shear layer filaments, instead of using a consistent orientation. In a second version of this method, local steering velocities were calculated along the mid-points of the shear layer, the thought being that these velocities would be more representative. However, none of these modifications worked to drive the model to convergence in sideslip. Generally speaking, high sideslip angles with low angles of attack proved the most challenging for the LOM.

A more involved idea was to build alternate geometries for the shear layer filaments and test which model would converge. Originally, the flat geometry of the shear layer was chosen for its simplicity and therefore lower computation time, however it was always understood that this representation was a rough approximation of the actual spiraling shape of the streamlines in the free shear layer. Therefore, in these new approximations, three different variations of a curve were designed: (i) a portion of a circle, the total turning angle of the flow chosen by the user, (ii) a specific portion of a circle, chosen by the LOM such that it is tangent to the local flow at each chordwise position along the wing-tip edge, and finally (iii) a spiral. In these designs any number of straight line segments, chosen by the user, can represent the curve. In the current work, 5 segments were used. After running all of these configurations, only two configurations consistently converged in sideslip: the 270° circle and the spiral. And, of these two, the 270° circle had the best rolling-moment agreement. Therefore, the 270° circle was validated for lift, drag and pitching moment as well. Drag and pitching-moment agreement were less close than for the planar shear layer, while lift was better predicted than the planar shear layer. Because this shear layer is more complex, and therefore more computationally expensive, this geometry is considered alternate and preliminary at this time. Therefore, these results are included in Appendix A.

Chapter 4

Conclusions

A low-order model designed both to model the free shear layer along wing tips and control the shedding of vorticity into that layer has been presented, discussed and validated against experimental work on low-aspect-ratio wings. The model is based on a conventional vortex lattice method model that has been augmented with additional vortex rings along each wing tip to model the free tip vortices and their feeding shear layers. Lift, drag and pitching-moment agreement are quite good. And, the spanwise and chordwise lift distributions suggest that the model is able to successfully capture the vortex lift that has an outsized effect on low-aspect-ratio wings. As of this writing, the current model, with its flat shear layer, fails to converge for most orientations in sideslip, and therefore, the model could not be validated against experimental rolling-moment results. The following addresses each of the objectives outlined in Chapter 1 and assesses how well each were met.

There were three main objectives set out for the LOM in the current work:

1) ***Achieve convergence of the model across a range of angles of attack and sideslip angles, and successfully demonstrate allocation of vorticity between what remains bound to the wing tip and what is shed to feed the free tip vortex***.

Although the model fails to converge for most cases with sideslip, the model did successfully meet the remainder of this objective. The model was shown to be able to "throttle" forces and moments by controlling how much vorticity may remain bound to the wing tip. A maximum lift capacity was demonstrated with a Γ_{crit} value of 0, with the total lift decreasing as Γ_{crit} increases. At a sufficiently large value of Γ_{crit}, at which the flow is modeled as fully-attached, it was shown that the LOM acted identically to a conventional VLM.

2) ***Accurately locate the tip vortices***.

As outlined in Chapter 1, this objective presented challenges inherent to any VLM that attempts to capture separated flow in the near vicinity of the wing. However, the LOM predicted the tip-vortex positions quite well. Tip-vortex locations at the trailing edge were compared to experimental work, an empirically-derived model and CFD results. It was shown that as Γ_{crit} increased, meaning more vorticity remained bound to the tip, the tip vortex moved inboard, consistent with the findings of the "Vortex Flow Experiment 2" [29] study of delta wing leading-edge geometries.

3) ***Accurately predict forces and moments***.

Lift, drag and pitching moment were fairly well predicted. Considering that prediction of moments is particularly sensitive to the locations of the suction forces associated with the tip vortices, and therefore the locations of the tip vortices, the LOM performed fairly well in predicting pitching moments. However, rolling-moment validation proved more challenging. The LOM in its current form, which uses a flat shear layer geometry, fails to converge for most cases in sideslip. In Appendix A, the results of an alternate shear layer geometry are presented.

REFERENCES

[1] Blair B. Gloss and T. Johnson, Forester. Development of an aerodynamic theory capable of predicting surface loads on slender wings with vortex flow. Technical Report NASA CP-001, National Aeronautics and Space Administration, Langley Research Center, Hampton, VA, 1977.

[2] Edward C. Polhamus. A concept of the vortex lift of sharp-edge delta wings based on a leading-edge-suction analogy. Technical Report NASA-TN D-3767, National Aeronautics and Space Administration, Ames Research Center, Moffett Field, CA, 1966.

[3] M.A. Engel. A wind tunnel investigation of a wing-tip trailing vortex. Master's thesis, Virginia Polytechnic Institute and State University, Department of Aerospace Engineering, 1995.

[4] Vernon J. Rossow. Lift-generated vortex wakes of subsonic transport aircraft. *Progress in Aerospace Sciences*, 35(6):507–660, 1999.

[5] Stergios I. Liapis and Gordon J. Follin. The structure and development of a wing-tip vortex. *Journal of Fluid Mechanics*, 312:67–106, 1995.

[6] S.C.C. Bailey and S. Tavoularis. Measurements of the velocity field of a wing-tip vortex, wandering in grid turbulence. *Journal of Fluid Mechanics*, 601:281–315, 2008.

[7] Nikolai Kornev and Nawar Abbas. Numerical Simulation of the tip vortex behind a wing oscillated with a small amplitude. *Journal of Aircraft*, 54(2):828–834, 2017.

[8] Adam C. DeVoria and Kamran Mohseni. On the mechanism of high-incidence lift generation for steadily translating low-aspect-ratio wings. *Journal of Fluid Mechanics*, 813:110–126, 2017.

[9] Joseph Katz and Allen Plotkin. *Low-Speed Aerodynamics*. Cambridge Aerospace Series. Cambridge University Press, Cambridge, UK, second edition, 2001.

[10] Michael S. Francis and Donald A. Kennedy. Formation of a Trailing Vortex. *Journal of Aircraft*, 16(3):148–154, 03 1979.

[11] J. D. Hoffman and H. R. Velkoff. Vortex flow over helicopter rotor tips. *Journal of Aircraft*, 8:9(9):739–740, 1971.

[12] Peiye Zhu, Wenxi Shou, and Shijun Luo. Nonlinear prediction of subsonic aerodynamic loads on wings and bodies at high angles of attack. *Computer Methods in Applied Mechanics and Engineering*, 26(3):305–319, 1981.

[13] Mook D.T. Kandil, O.A. and A.H. Nayfeh. A numerical technique for computing subsonic flow past three dimensional canard-wing configurations with edge separations. 77(1), 1977.

[14] S. Dodbele and A. Plotkin. Prediction of vortex lift on interacting delta wings in incompressible flow. *Journal of Aircraft*, 21(7):451–452, 1984.

[15] P. Kondstadinopoulos, D. F. Thrasher, D. T. Mook, A. H. Nayfeh, and L. Watson. A vortex-lattice method for general, unsteady aerodynamics. *Journal of Aircraft*, 22(1):43–49, 1985.

[16] C.E. Brown and Jr. W.H. Michael. Effect of leading-edge separation on the lift of a delta wing. *Journal of the Aeronautical Sciences*, 21:690–694, 1954.

[17] Daniel Levin and Joseph Katz. Vortex-lattice method for the calculation of the nonsteady separated flow over delta wings. *Journal of Aircraft*, 18(12):1032–1037, 1981.

[18] S. M. Belotserkovskii. Calculation of the flow around wings of arbitrary planform over a wide range of angles of attack. *Fluid Dynamics*, 3(4):20–27, Jul 1968.

[19] Jaime G. Wong, Graeme Gillespie, and David E. Rival. Circulation redistribution in leading-edge vortices with spanwise flow. *AIAA Journal*, 56:3857–3862, 2019.

[20] Charles P. Ellington, den B. van, Alexander P. Willmott, and Adrian L. R. Thomas. Leading-edge vortices in insect flight. *Nature*, 384(6610):626–630, Dec 1996. Copyright - Copyright Macmillan Journals Ltd. Dec 19-26, 1996; Last updated - 2017-10-31; CODEN - NATUAS.

[21] Iman Borazjani and Mohsen Daghooghi. The fish tail motion forms an attached leading edge vortex. *Proceedings of the Royal Society B: Biological Sciences*, 280(1756):2012–2071, 2013.

[22] J. Videler, E. Stamhuis, and G. Povel. Leading-edge vortex lifts swifts. *Science*, 306(5703):1960–1962, 2004.

[23] John E. Lamar. Extension of Leading-Edge-Suction Analogy to Wings with Separated Flow Around the Side Edges at Subsonic Speeds. NASA TR NASA-TR R-428, National Aeronautics and Space Administration, Langley Research Center, Hampton, VA, 1974.

[24] John E. Lamar. Prediction of vortex flow characteristics of wings at subsonic and supersonic speeds. *Journal of Aircraft*, 13(7):490–494, 1976.

[25] Smith C. W. Bradley, R. G. and I. C. Bhateley. Vortex-lift prediction for complex wing planforms. *Journal of Aircraft*, 10(6):379–381, 1973.

[26] John E. Lamar. Effects of wing leading edge radius and reynolds number on longitudinal aerodynamic characteristics of highly swept wing-body configurations at subsonic speeds. NASA TN NASA-TN D-8361, National Aeronautics and Space Administration, Langley Research Center, Hampton, VA, 1976.

[27] N.A. Chigier and V.R. Corsiglia. Tip Vortices - Velocity Distributions. NASA TM NASA-TM-X-62,087, National Aeronautics and Space Administration, Ames Research Center, Moffett Field, CA, 1971.

[28] Kiran Ramesh, Ashok Gopalarathnam, Kenneth Granlund, Michael V. Ol, and Jack R. Edwards. Discrete-vortex method with novel shedding criterion for unsteady airfoil flows with intermittent leading-edge vortex shedding. *Journal of Fluid Mechanics*, 751:500–538, 2014.

[29] James M. Luckring. Initial experiments and analysis of blunt-edge vortex flows for vfe-2 configurations at Nasa Langley, USA. *Aerospace Science and Technology*, 24(1):10–21, 2013.

[30] Adam C. DeVoria and Kamran Mohseni. A vortex model for forces and moments on low-aspect-ratio wings in side-slip with experimental validation. *Proceedings of the Royal Society of London Series A, Physical and Engineering Sciences*, 473(2198):20160760, 2017.

[31] Kunihiko Taira and Tim Colonius. Three-dimensional flows around low-aspect-ratio flat-plate wings at low reynolds numbers. *Journal of Fluid Mechanics*, 623:187–207, 2009.

[32] Peter H. Cosyn and Jan Vierendeels. Numerical investigation of low-aspect-ratio wings at low reynolds numbers. *Journal of Aircraft*, 43(3):713–722, 2006.

[33] B. R. Ramaprian and Youxin Zheng. Measurements in rollup region of the tip vortex from a rectangular wing. *AIAA Journal*, 35(12):1837–1843, 1997.

APPENDIX

Appendix A

The LOM in its current form, which uses a planar shear layer geometry, fails to converge for most cases in sideslip. Therefore, in this appendix, the results for an alternate shear layer geometry are presented. In this version, the free tip vortices are still "steered" by local velocities to follow a streamline. However, the single straight-line shear layer segments are replaced with three-quarter-circles (Figure A.1). In all cases presented, 5 line segments were used to represent the curve. Although still a very rough approximation of the actual flow direction, this geometry is a somewhat higher fidelity representation. One slight modification was made to prevent any segments from falling below the plane of the wing, since this would represent an unrealistic flow pattern. In these cases, the program is set to force what segments lie below this plane to lie in the plane of the wing.

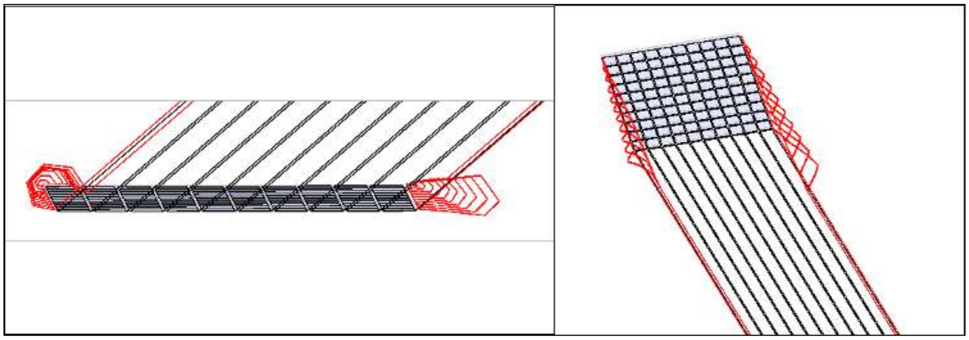

Figure A.1: Bound (conventional VLM) and free (supplementary) vortex filaments in alternate 3/4-circle shear layer geometry for uncambered wing, $\mathcal{R} = 1$, $\alpha = 10°$, $\beta = -5°$. Left: viewed from rear, in chordwise direction; Right: viewed from above.

A.1 Tip-vortex Locations

First, a qualitative comparison of tip-vortex positions in sideslip is presented. Figure A.2 presents the relative positions of the tip vortices, demonstrating a lower and more inboard position of the tip vortex on the upstream side of the wing, consistent with the findings of DeVoria and Mohseni.

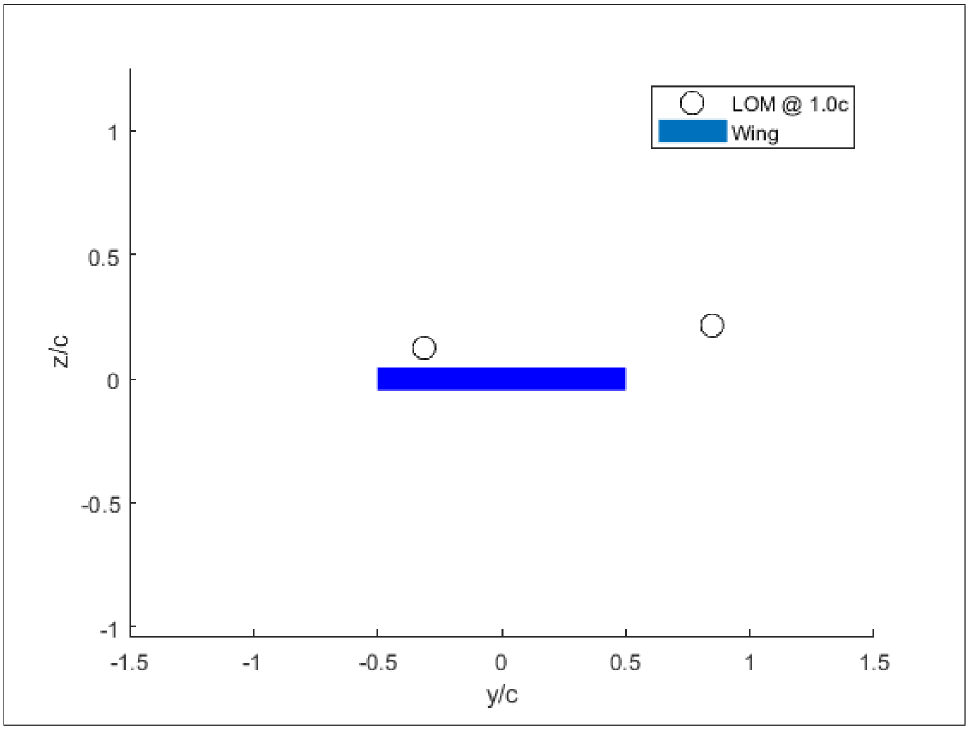

Figure A.2: Tip-vortex positions for an uncambered wing in sideslip; $\alpha = 25°$, $\beta = -35°$, $AR = 1$.

Next, tip-vortex positions for the $AR = 3$ and $AR = 8$ wings at multiple Γ_{crit} values are presented in Figure A.3 and Figure A.4, respectively. Generally, the predictions are slightly better than for the planar wing. Furthermore, the higher Γ_{crit} value predictions are closer to the baseline locations, which is more consistent with what would be expected for thicker wings. The $AR = 3$ wing and $AR = 8$ wing have thicknesses of 12% and 15%, respectively, well over the 4.2%

thickness of the flat plates used by DeVoria and Mohseni. Because a Γ_{crit} value of 0 gave the best results for those thin plates, a non-zero value of Γ_{crit} would be expected to better-predict the tip-vortex locations for these thicker wings.

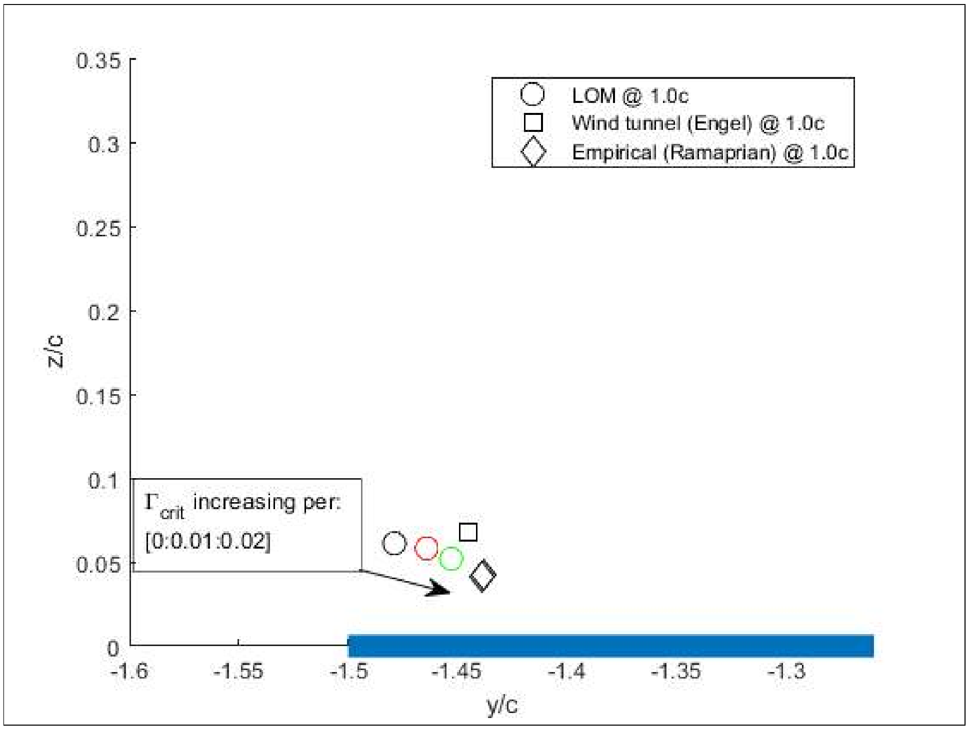

Figure A.3: Left wing-tip vortex positions for wing with NACA 0012 airfoil, Æ of 3, α of 7.5°, β of 0°, at a Reynolds number of 335,000 in Engel's work [3]; 10 chordwise lattices and 30 spanwise lattices used. Wing represented by blue line.

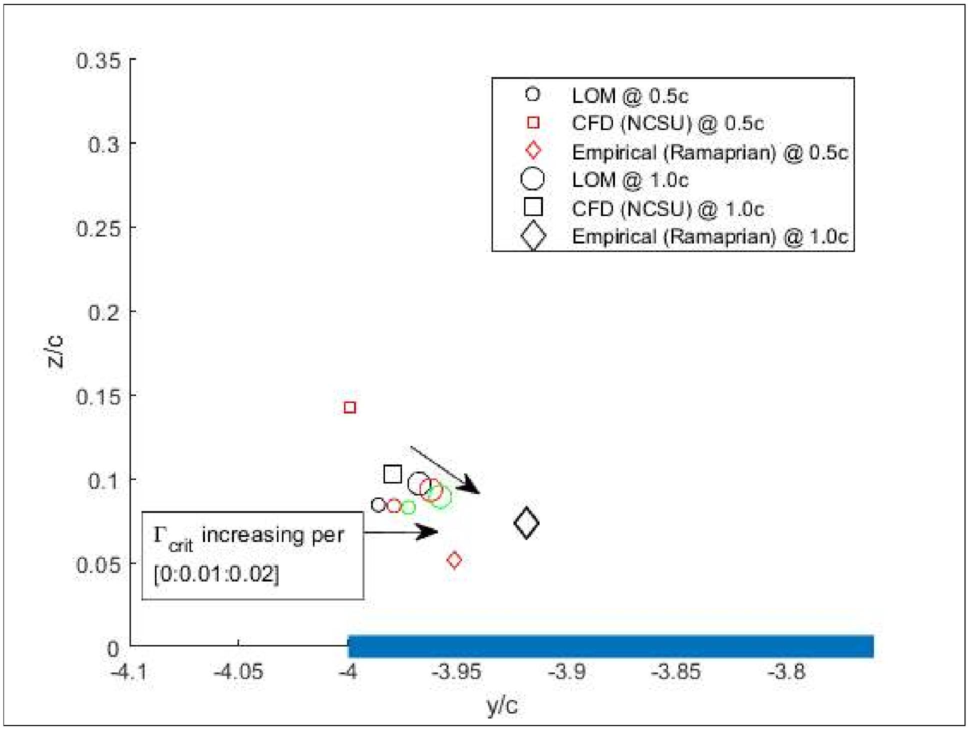

Figure A.4: Left wing-tip vortex positions for wing with NACA 4415 airfoil, Æ of 8, α of 12°, β of 0°, at a Reynolds number of 3×10^6 in in CFD work performed at NCSU; 10 chordwise lattices and 80 spanwise lattices used. Wing represented by blue line.

A.2 Study: Effect of Γ_{crit} on Forces and Moments

Just as for the planar shear layer, Figure A.5 demonstrates that (i) the forces and moments can be "throttled" by controlling the maximum allowable vorticity along the wing tips, and (ii) as Γ_{crit} increases, the predictions approach and then coincide with the conventional VLM predictions.

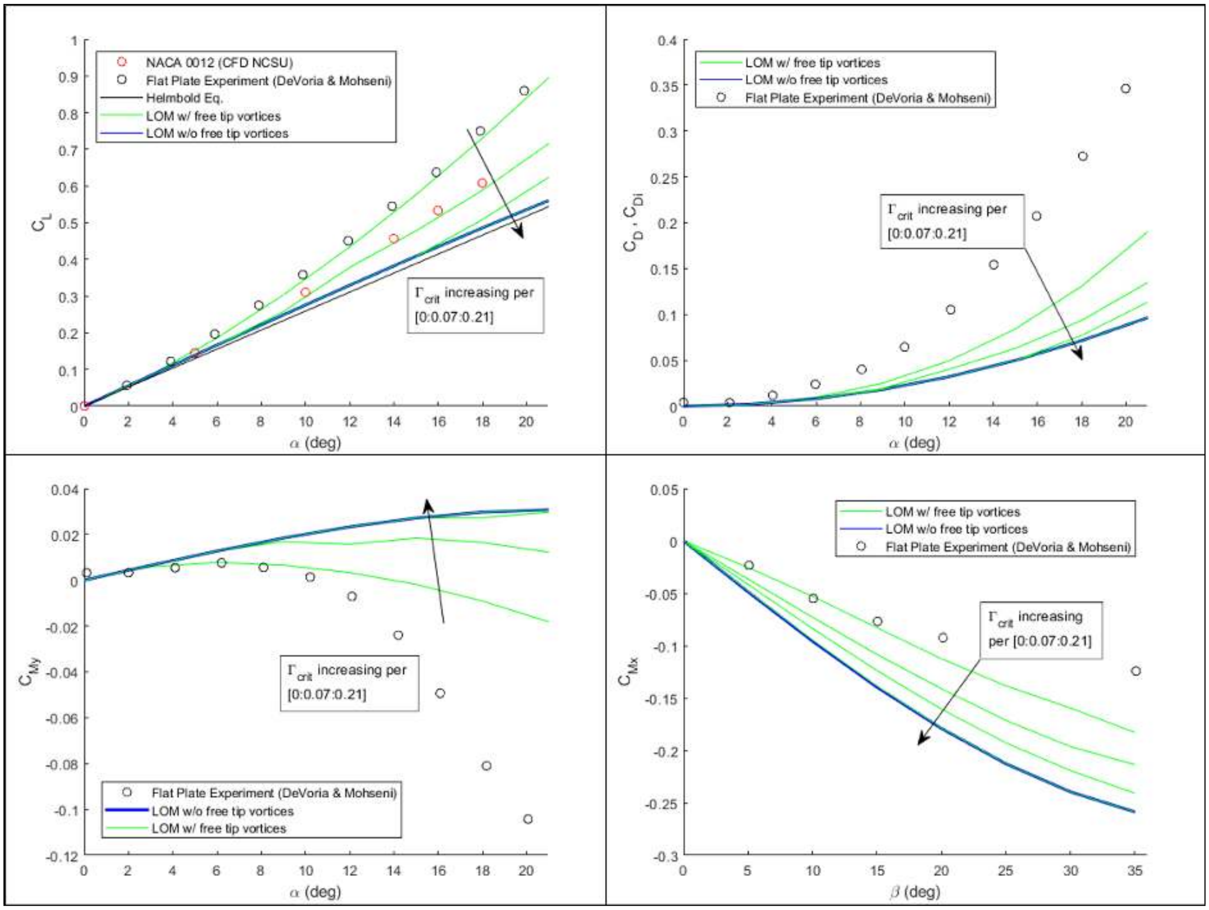

Figure A.5: Forces and moments with increasing Γ_{crit}, demonstrating that predictions approach and then coincide with conventional VLM results as Γ_{crit} increases; Æ$R = 1$, 10 chordwise lattices, 10 spanwise lattices, $\beta = 0°$.

A.3 Study: Effect of Number of Chordwise Lattices on Forces and Moments

In contrast to the planar shear layer, the forces and moments predicted by the LOM with the curved shear layer geometry do properly converge as the number of chordwise lattices increases. Figure A.6 demonstrates that 10 chordwise lattices produces reasonably converged results for all forces and moments.

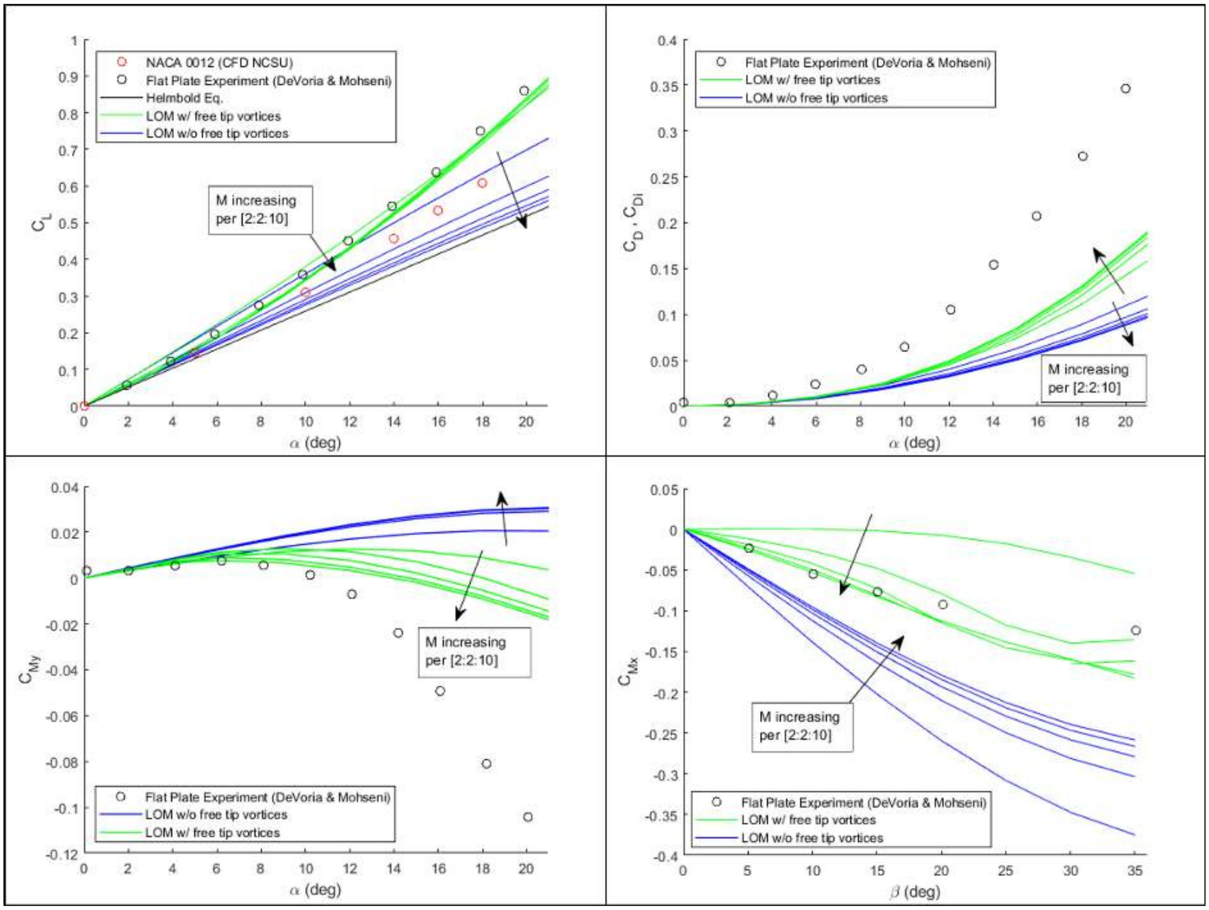

Figure A.6: Forces and moments with number of chordwise lattices, M, increasing per: 2,4,6,8 and 10. $\Gamma_{crit} = 0$, no sideslip.

A.4 Effect of Number of Spanwise Lattices on Forces and Moments

To an even greater degree than the planar shear layer geometry, the forces and moments predicted by the LOM with the curved shear layer geometry do properly converge as the number of spanwise lattices increases (as defined by the lattice Æ). Figure A.7 demonstrates that a lattice Æ of one produces reasonably converged results for all forces and moments.

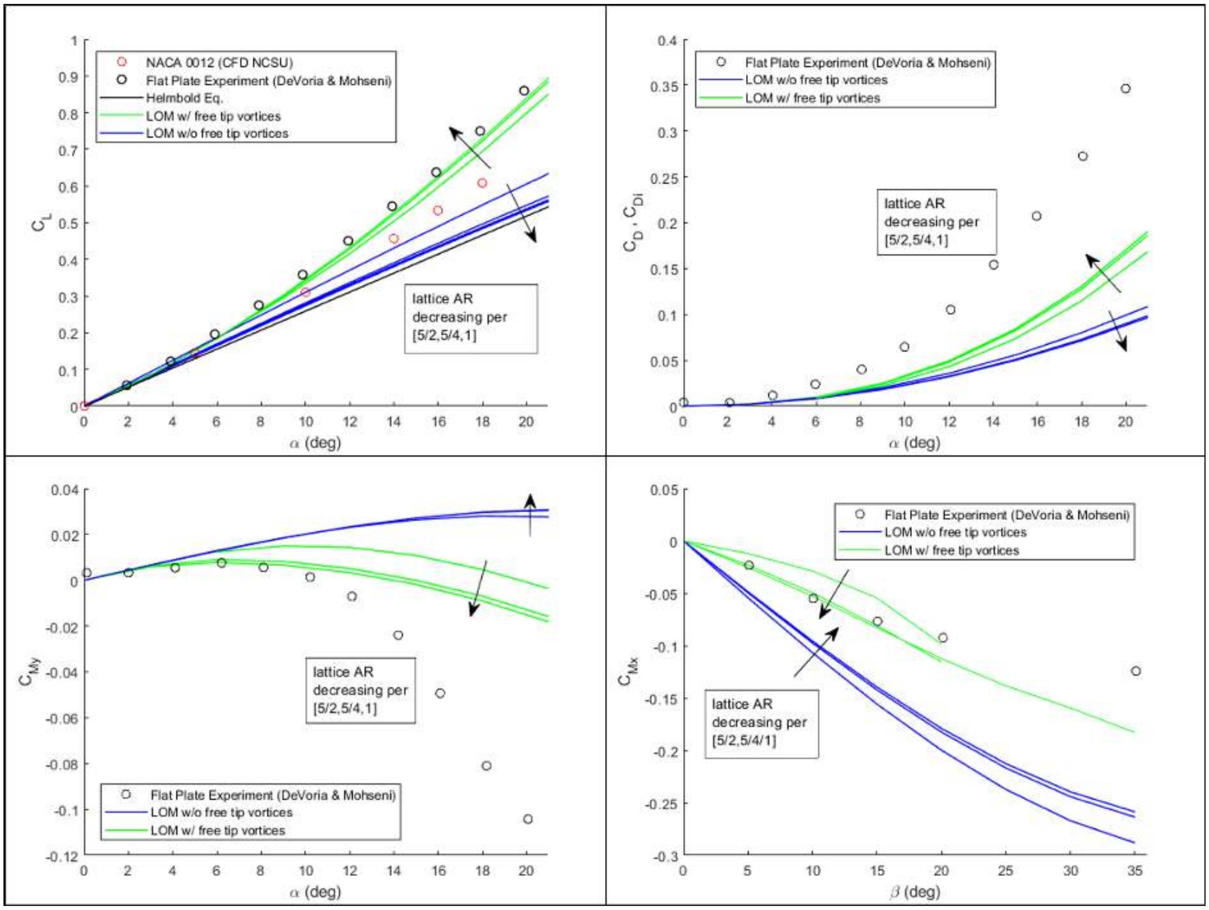

Figure A.7: Forces and moments predicted by the LOM with multiple values of the number of spanwise lattices, N, as defined by the lattice Æ; M = 10, Æ = 1, $\Gamma_{crit} = 0$. Missing LOM predictions for rolling moment are due to failure to converge.

A.5 Study: Effect of Æ on Spanwise Lift Distributions

As for the planar shear layer geometry, the curved shear layer geometry produces the expected lift distributions consistent with variations in Æ, Γ_{crit}, α, and β.

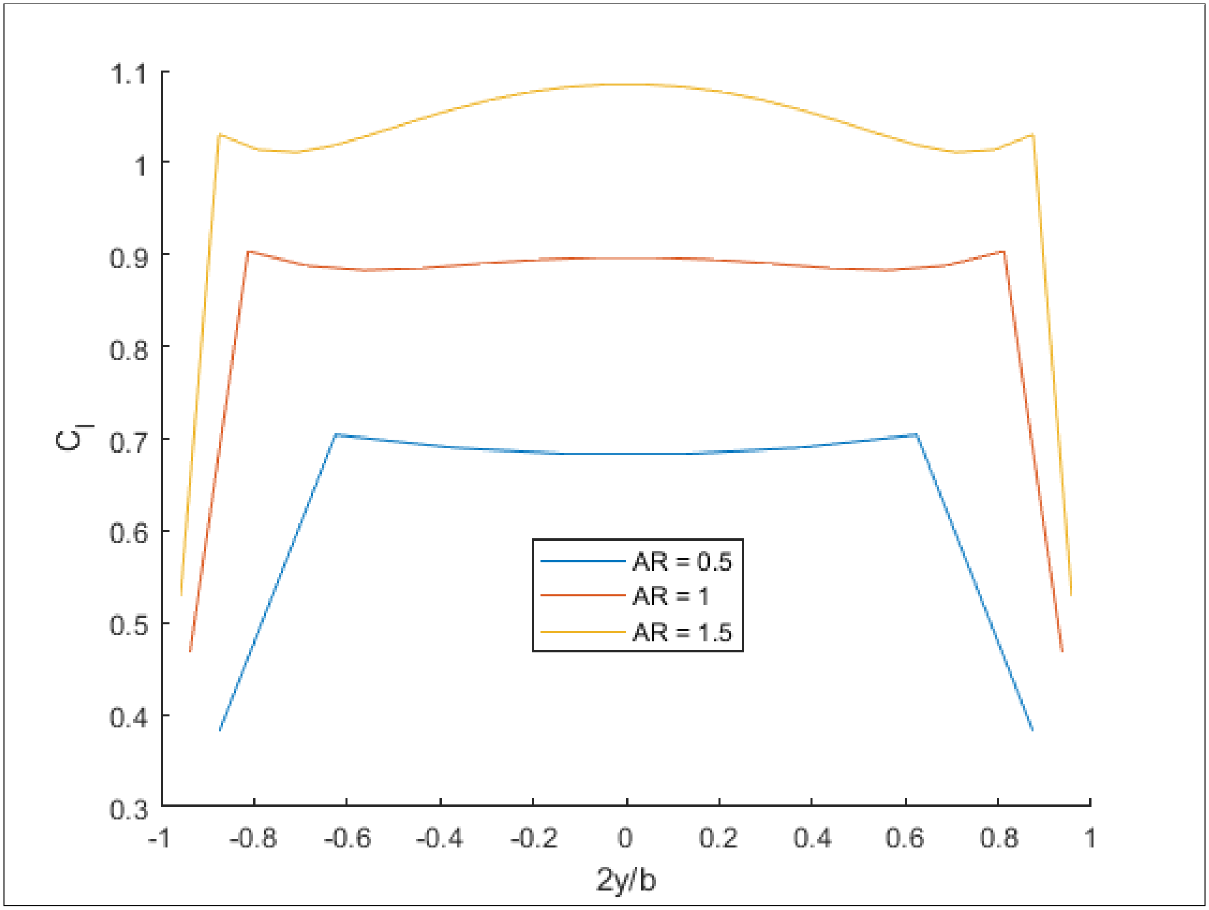

Figure A.8: Spanwise lift distributions from LOM for uncambered wings at multiple Æs, Γ_{crit} = 0, $\alpha = 21°$, $\beta = 0°$, 10 chordwise panels, lattice Æ = 0.625.

A.6 Correlating Lift Distributions with Lift Curves

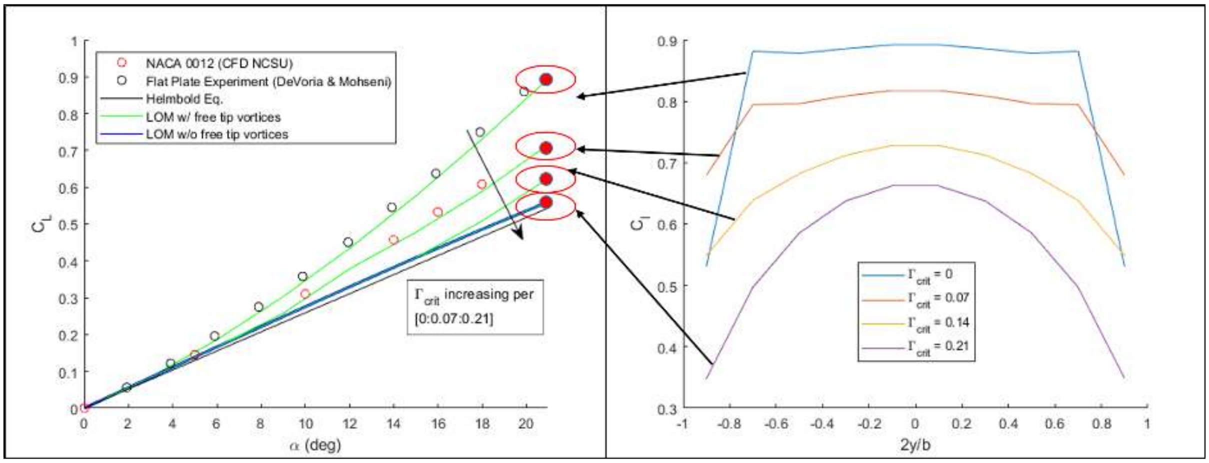

Figure A.9: Spanwise lift distributions for an uncambered wing at multiple Γ_{crit} values, Æ $=$ 1, $\alpha = 21°$, $\beta = 0°$, 10 chordwise panels, 10 spanwise panels.

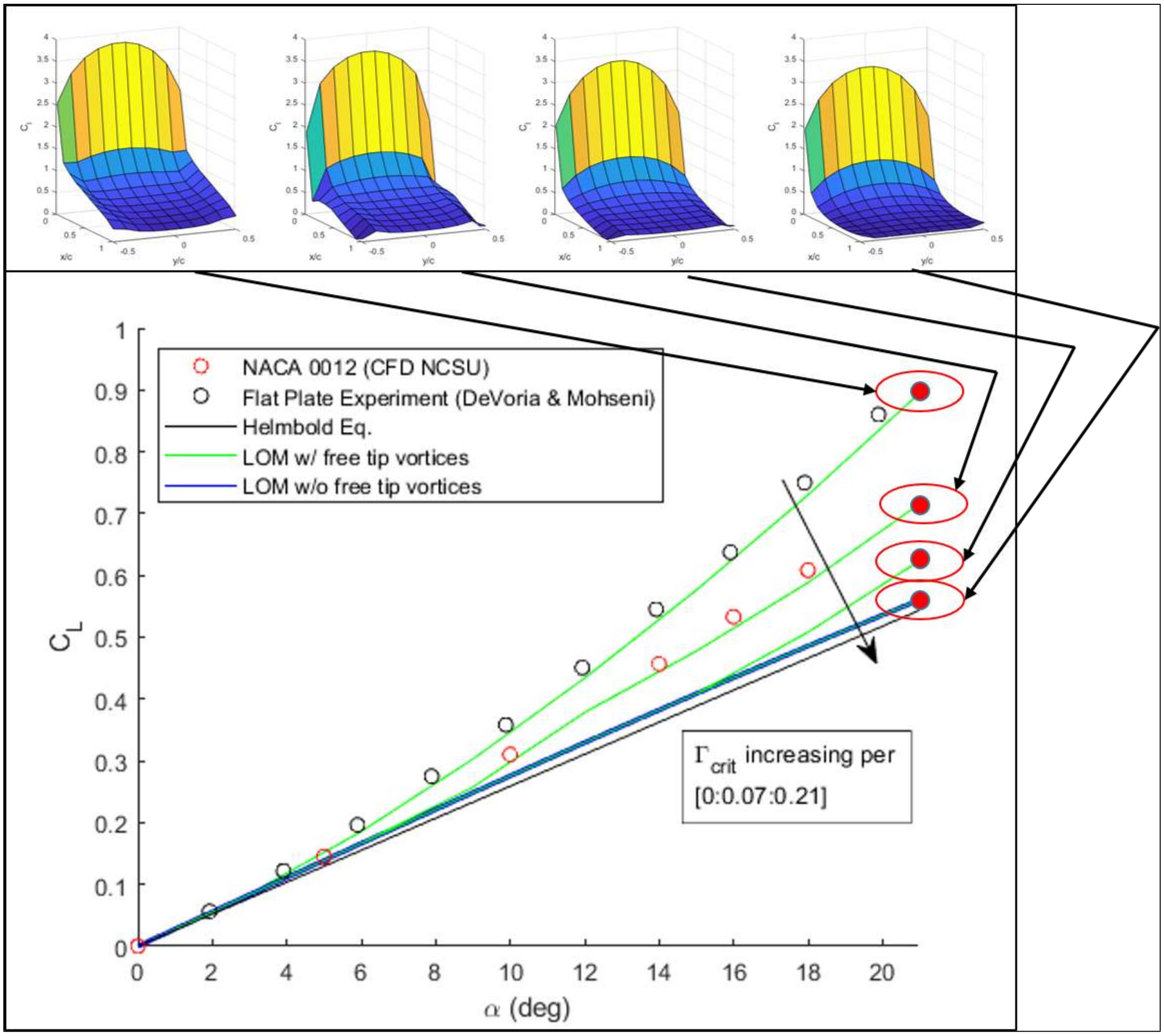

Figure A.10: Spanwise and chordwise lift distributions for an uncambered wing at multiple Γ_{crit} values, $A\!\!R = 1$, $\alpha = 21°$, $\beta = 0°$, 10 chordwise panels, 10 spanwise panels.

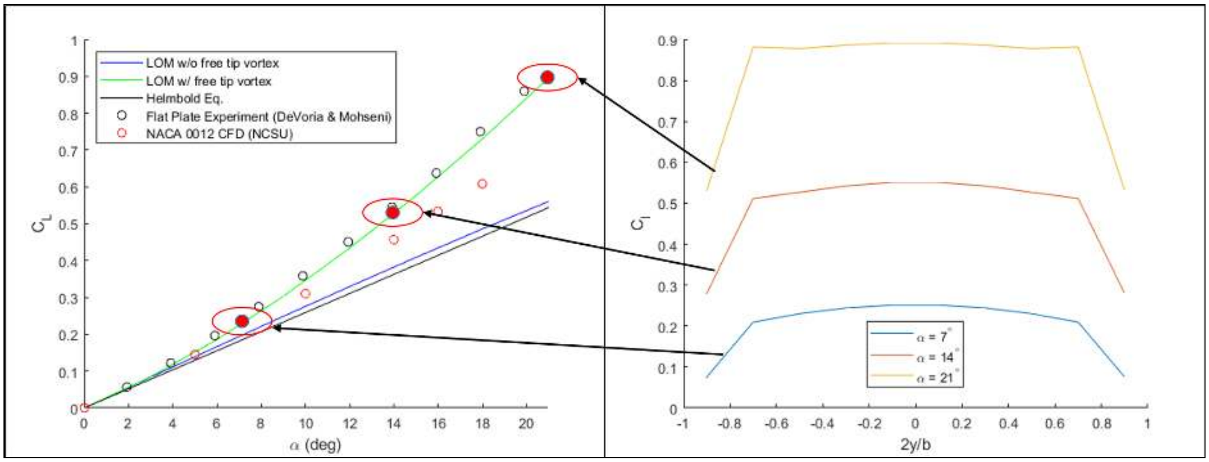

Figure A.11: Spanwise lift distributions for an uncambered wing at multiple angles of attack, $\Gamma_{crit} = 0$, $\AE = 1$, $\beta = 0^\circ$, 10 chordwise panels, 10 spanwise panels.

A.7 Lift Distributions with Sideslip

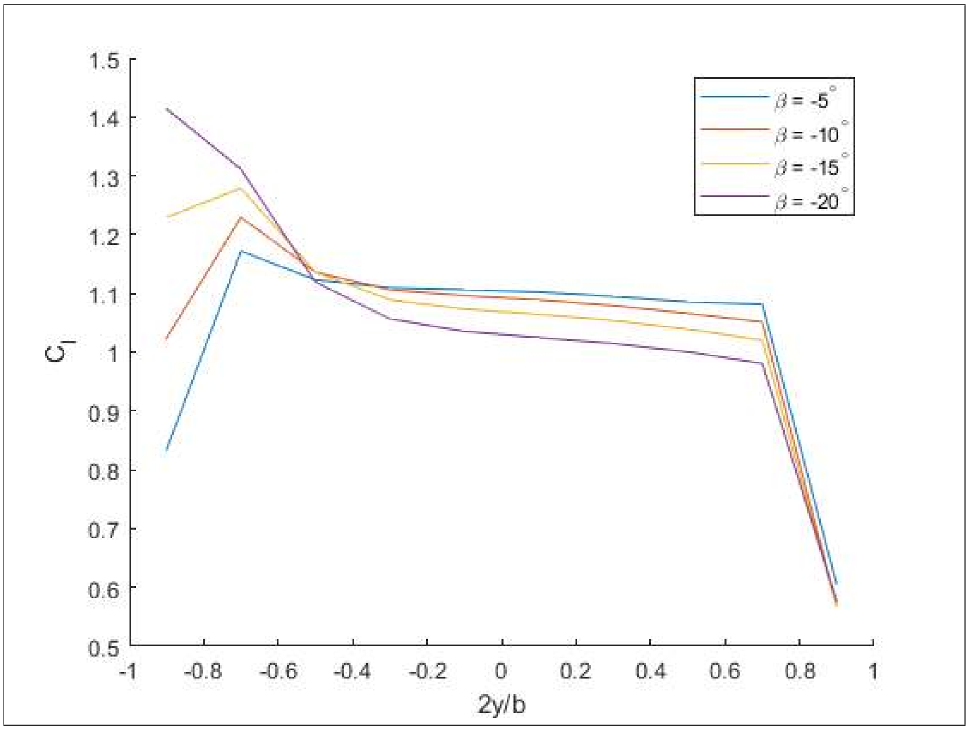

Figure A.12: Spanwise lift distributions for an uncambered wing at multiple β values, $AR = 1$, $\alpha = 25°$, $\Gamma_{crit} = 0$, 10 chordwise panels, 10 spanwise panels.

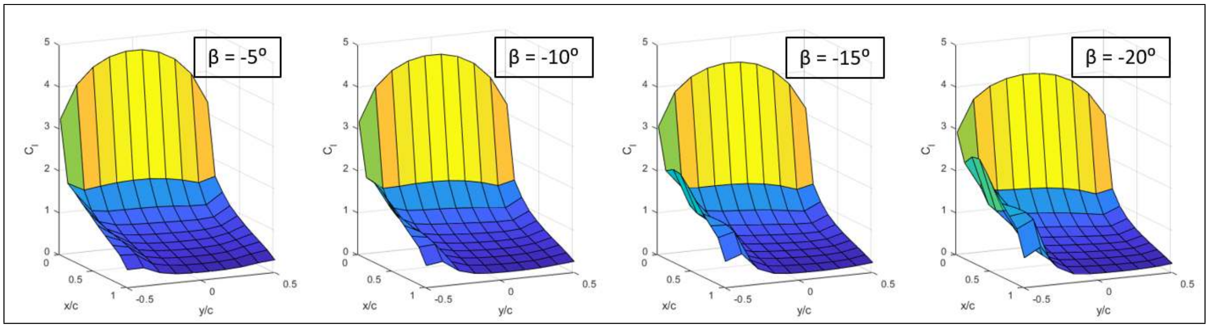

Figure A.13: Spanwise and chordwise lift distributions for an uncambered wing at multiple β values, $AR = 1$, $\alpha = 25°$, $\Gamma_{crit} = 0$, 10 chordwise panels, 10 spanwise panels.

A.8 Validation: Forces and Moments

The following sections present validations of lift, drag, pitching-moment, and rolling-moment results against those from DeVoria and Mohseni's experimental work. Lift, drag and pitching-moment agreement are similar to that of the planar geometry. The lift agreement is better, while the drag and pitching moment agreement is not as close. For rolling moment, not only is convergence achieved (unlike for the planar shear layer), but the agreement is quite good.

A.8.1 Validation: Lift

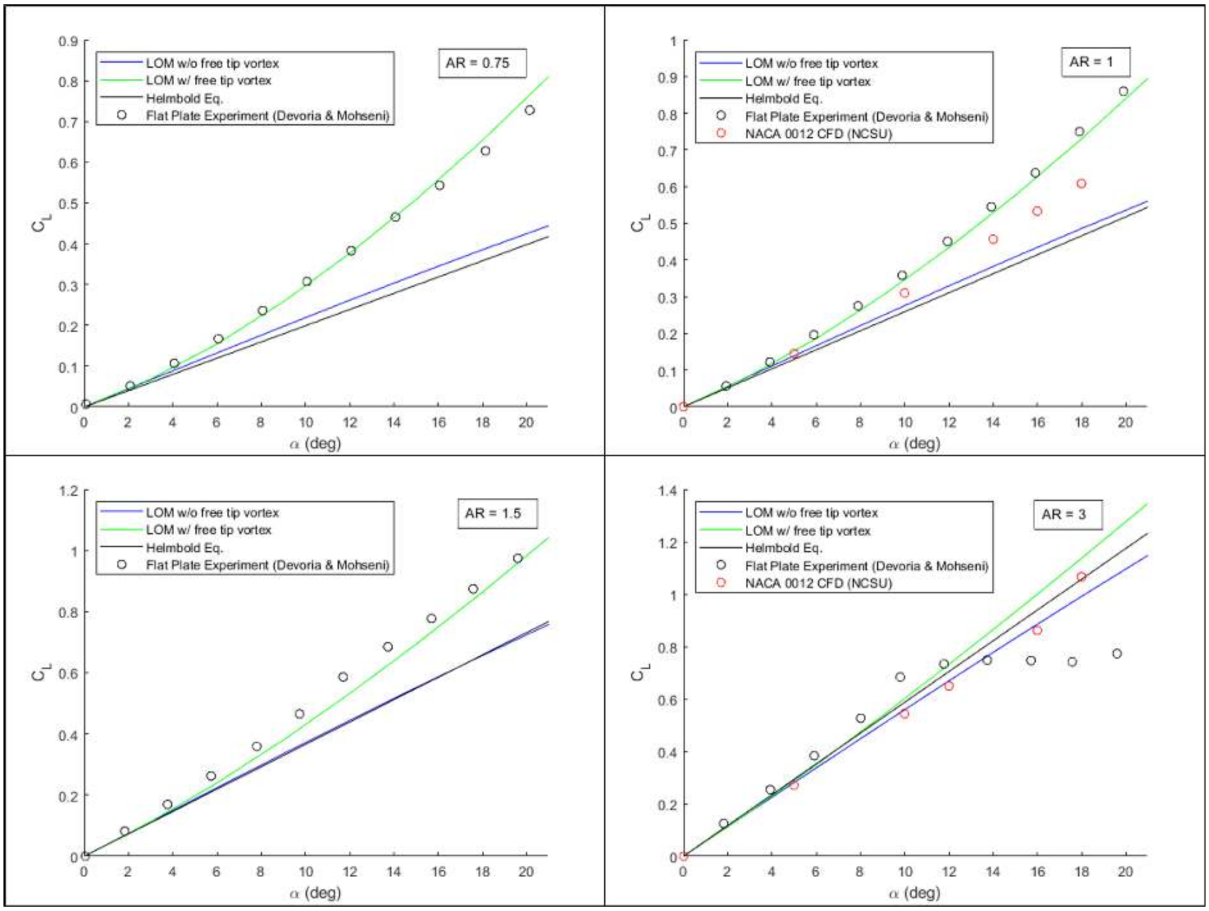

Figure A.14: C_L versus α, $\Gamma_{crit} = 0$, no sideslip, AR = 0.75, 1, 1.5 and 3.

A.8.2 Validation: Drag

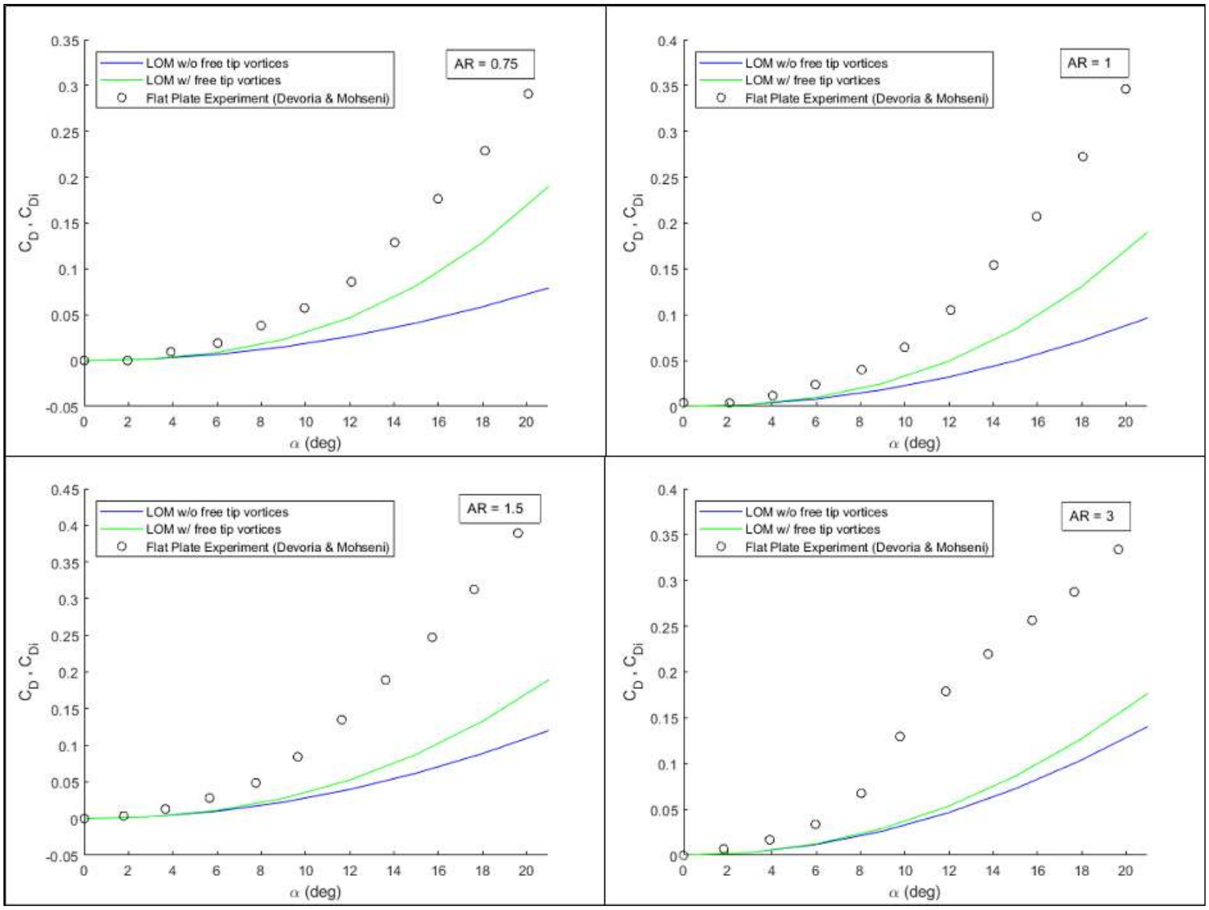

Figure A.15: C_D / C_{Di} versus α, $\Gamma_{crit} = 0$, no sideslip, AR = 0.75, 1, 1.5 and 3.

A.8.3 Validation: Rolling Moment

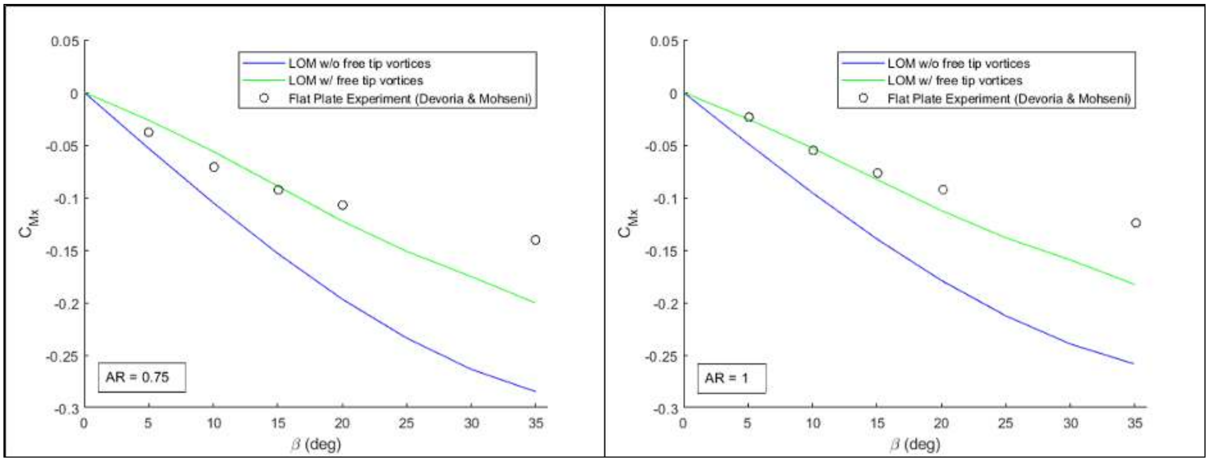

Figure A.16: C_{Mx} versus β, $\alpha = 25°$, $\Gamma_{crit} = 0$, AR = 0.75 and 1.

A.8.4 Validation: Pitching Moment

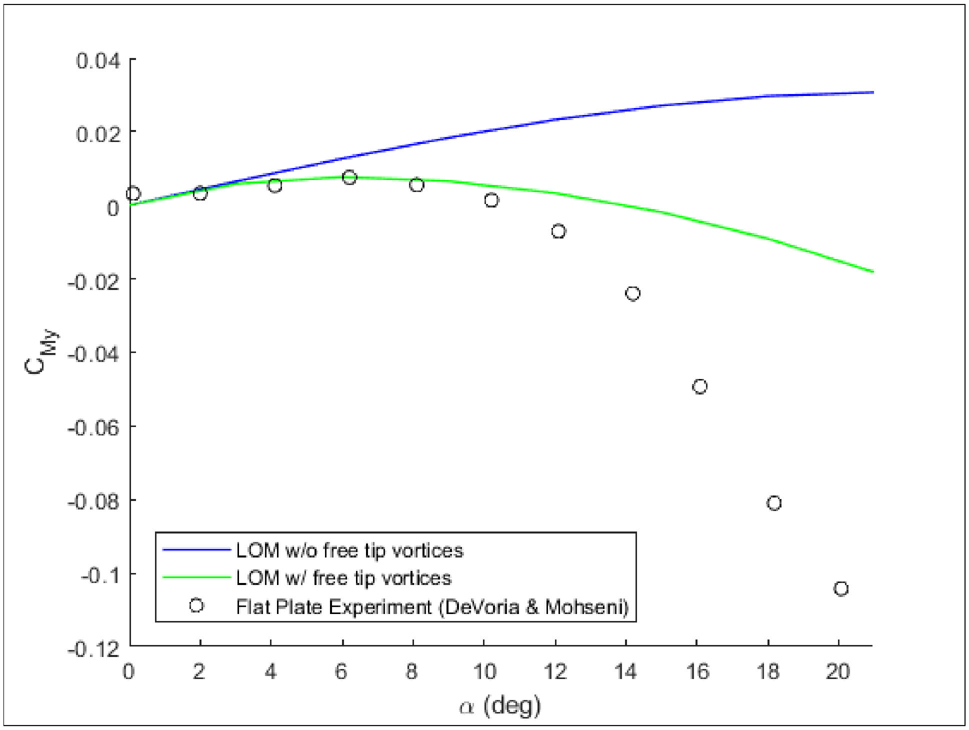

Figure A.17: C_{My} versus α, $\Gamma_{crit} = 0$, no sideslip, AR = 1.